UNIVERSITY OF CALIFORNIA
RIVERSIDE

Optical Injection of Spin Polarized Electrons in Silicon

A Dissertation submitted in partial satisfaction
of the requirements for the degree of

Doctor of Philosophy

in

Physics

by

John Harlan Muse

March 2018

Dissertation Committee:
Dr. Harry Tom, Chairperson
Dr. Allen Mills
Dr. Umar Mohideen

The Dissertation of John Harlan Muse is approved:

_____

_____

_____

Committee Chairperson

University of California, Riverside

ACKNOWLEDGEMENTS

I would like to thank Dr. Tom for giving me the opportunity to work on this important topic. I would also like to thank my committee members, Dr. Mohideen and Dr. Mills, for their help.

I would also like to thank the collaborators on this project: Dr. Koji Yokoyama, Dr. Allen Drew, Dr. James Lord, Dr. Francis Pratt, Jingliang Miao, and Prashantha Murahari who are all in the United Kingdom.

ABSTRACT OF THE DISSERTATION

Optical Injection of Spin Polarized Electrons
in Silicon

by

John Harlan Muse

Doctor of Philosophy, Graduate Program in Physics
University of California, Riverside, March 2018
Dr. Harry Tom, Chairperson

Silicon is a popular semiconductor in spintronics. Advancements in research into this material has only happened through contacts. There hasn't been any research done by means of optical injection due to its indirect bandgap. In this dissertation, I demonstrate the optical injection of spin polarized electrons into silicon using a muon spin relaxation technique that utilizes spin-polarized muons to probe for conduction electron spin polarization.

When an antimuon, a positive muon, is implanted into a semiconductor, it captures a conduction electron and forms a muonium atom. The spin of the electron can either be parallel or antiparallel to the muon spin. If the spin is parallel, the spins are fixed. But, if the spins are antiparallel, then they are in a superposition of both configurations; muon spin-up with electron spin-down plus muon spin-down plus

electron spin-up. This spin flipping is the basis of how the muons can probe for the conduction electron spin polarization.

The experiment was completed on both n-type and intrinsic silicon to prove the existence in two different types. The wavelength was scanned over an interval slightly above the bandgap since there is virtually no absorption at the bandgap. Since silicon is an indirect bandgap, the photons alone can't be absorbed into the bottom of the bandgap due to the momentum shift, so phonons are required to either be absorbed or emitted to preserve momentum conservation. Due to the low temperature of the experiment, phonon emission is the only practical path for absorption. Several parameters, including wavelength, applied magnetic field, and laser power, were varied to find the and analyze signal. The experiment was carried out over the course of several years, and trips, to the ISIS pulsed muon source with a successful detection of the conduction electron spin polarization in both the n-type and intrinsic silicon samples.

Contents

List of Figures

List of Tables

Chapter 1

Introduction

Spintronics experiments in silicon (Si) dates back to 1968 when Lampel [1] performed an experiment in which a Si sample was illuminated with circularly polarized light and the resulting dynamic nuclear polarization was measured. This demonstrated that a non-equalibrium of spin-polarized electrons was created. However, the amount was low and was deemed inefficient. It wasn't until almost 40 years later, in 2007, when Appelbaum [2] demonstrated spin injection in Si via electrical injection. Prior to this, it had only been shown in direct bandgap materials [3, 4, 5]. Later in 2007, Jonker's experiment [6] used a quantum tunnel barrier to inject spin into a Si diode. The experiment observed the emission of circularly polarized light of which showed a spin polarization of about 10%. An estimate of about 30% spin polarization of electrons at 5K was achieved through rate equations. A few years later Cheng [7] published the theory of optical spin orientation in Si, which showed the well defined selection rules which can yield up to 25% spin polarization. This experiment is done using a relatively new technique of probing spin polarization using antimuons as a spin probe. So far, the only experiments that have shown spin injection into Si, or any indirect bandap semiconductor, has been through the use of contacts. There have

been many experiments that have shown spin inection through optical means [8, 9, 10] for direct bandgap materials, but there haven't been any for indirect bandgap. This experiment will show optical spin injection into Si and detection with the use of Muon Spin, Rotation, Relaxation, and Resonance (μSR) techniques.

μSR is a set techniques that are used to probe materials to gather information at the atomic level. Of the many different techniques lumped into this category, the usage of antimuons to probe the spin polarization of conduction band electrons in semiconductors is what will be used here. This technique, which was first proposed by Torekai [11], involves the implantation of an antimuon into the material of interest, in this case Si. While inside the sample, the antimuon will capture an electron to form an exotic atom called muonium (Mu). Since the lifetime of the antimuon is 2.2 μs, the atom is short-lived. However, it still has a longer spin lifetime than a conduction-band electron in Si, which can be up to 1 μs in cold, undoped samples [12]. Hyperfine coupling will exist between the antimuon and electron and it will be either in a triplet state (S=1) or a singlet state (S=0). When the spin of the antimuon and electron have parallel spin, they can add/subtract to the overall signal. When they have anti-parallel spin, they will be in a superposition that flips the spin of both particles causing them to show up in the detected signal. Therefore, this method can detect a difference in the amount of spin up and spin down conduction band electrons.

Torekai [11] used a sample comprised of gallium arsenite (GaAs), gallium arsenite phosphide (GaAsP), and Si layers. Spin-polarized electrons were then injected into the conduction band of the GaAs layer. Spin polarized electrons were then injected into the conduction band of the GaAs layer by means of a laser and traveled into the Si layer. The antimuons were injected into the Si layer. The results were promising and warranted further study. Yokoyama [9] continued to test viability of this technique by detecting the degree of spin polarization (DSP) of the conduction band electrons

in an n-type GaAs sample, a semiconductor in which the spin polarization of the conduction band electrons have been measured, with a known method of two-color time resolved kerr rotation (TRKR). Then, the μSR was done using a laser of the same wavelength to inject the spin polarized electrons into the conduction band while utilizing the same principles of the μSR techniques that Torekai used. The results of the TRKR experiment confirmed the existance of the DSP of the conduction-band electrons. The results of the μSR experiment also showed the existance of the GaAs DSP, proving the validity of this μSR technique as a probe for finding the DSP of the conduction band electrons.

Since this μSR technique has been proven to work with GaAs, it will now be used to find the DSP of the conduction band electrons of Si. The results of this experiment have shown the existance of a DSP of conduction band electrons in Si through the injection of spin from an all optical source. The experiment was done over several runs at the ISIS Pulsed Muon Facility at different laser intensities, different magnetic fields, different laser wavelengths and two different samples, both which showed the signal of interest.

Chapter 2

Silicon

2.1 Silicon Band Structure

Figure 2.1 shows the band structure of Si. The valence band maxima lie at the Γpoint at k=(0,0,0) while the conduction band minimum lies along the $\triangle_k$ path about 85% of the way from the Γ point to the X point (see Figure 2.2). There are six equivalent valleys $(X, \bar{X}, Y, \bar{Y}, Z, \bar{Z})$ located along x,y, and z axes as shown in Figure 2.3. The oblong shape is due to the asymmetry of the effective mass. The Heavy Hole (HH) and Light Hole (LH) valence band maxima lie at E=0eV while the Split Off (SO) band is located 44meV lower. The indirect band gap is $E_g = 1.17eV$ at $T = 0K$ while a direct bandgap is $E_{dg} = 3.4eV$.

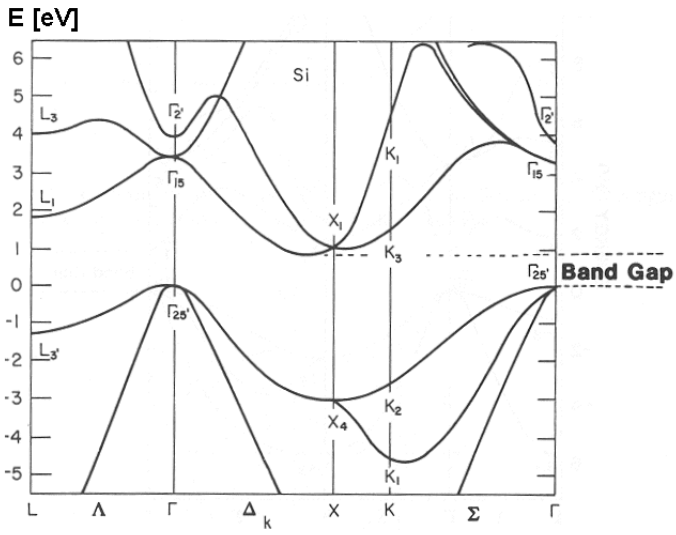

Figure 2.1: Si Bandgap Structure.[13]

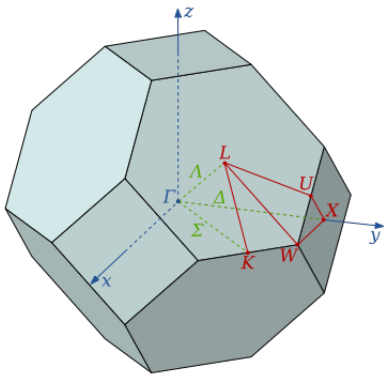

Figure 2.2: Brillouin Zone of Si showing notable locations within the lattice [14].

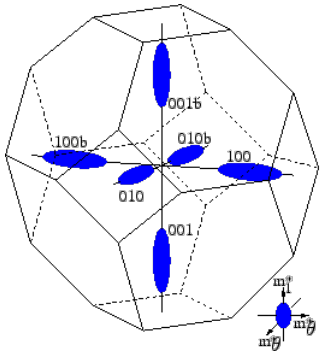

Figure 2.3: Brillouin Zone of Si showing all $(X, \bar{X}, Y, \bar{Y}, Z, \bar{Z})$ valleys [15].

2.2 Silicon Lifetime

The spin lifetime in Si has usually been thought to be caused by the Elliott-Yafet [16, 17] mechanisms. Each mechanism individually only makes up a fraction of the measured spin lifetimes, but together add up to close to what the measurements show, as shown in Figure 2.4(a). Cheng [7] performed a comprehensive investigation of the spin lifetimes in undoped Si. The results show that the Si spin lifetimes is dominated by intraband phonon scattering at temperatures lower than 120K and by interband scattering at temperatures above 120K as shown in Figure 2.5(b). Since the intraband dominate below 120K, the prediction by Yafet of the spin lifetime following $T_{1,intra} \sim T^{-\frac{5}{2}}$works well, but when the temperature rises above 120K, it is no longer valid. Cheng's work shows that a better prediction follows $T_1 \sim T^{-3}$. Figure 2.5 shows this prediction follows the experimental work by Appelbaum [2] in which the Si lifetime was measured through spin injection of hot electrons into the Si; the electrons were accelerated through the sample with an electric field and their spin was measured after they were transported to the other side. The prediction also fits well with electron spin resonance (ESR) measurements by Lepine [18] and Lancaster [19]. The lowest temperature shown is 60K for this method since lower temperatures are prevented by carrier freeze out effects. The lifetime here is about $1\mu s$.

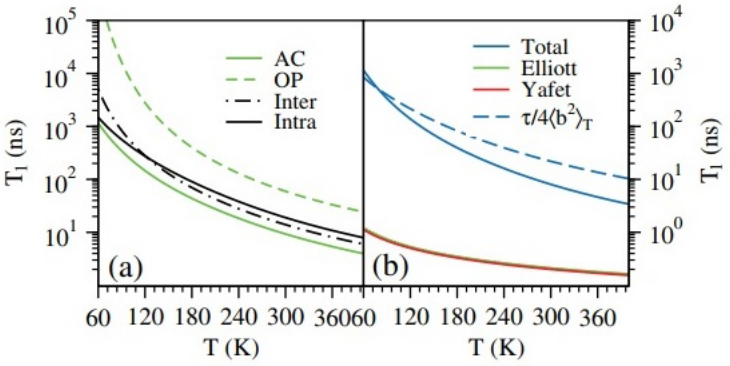

Figure 2.4: Analysis of Spin Relaxation in Si [7]. (a) shows the phonon contributions to the spin lifetime calculations. (b) shows the spin lifetime calculations from both Elliot and Yafet mechanisms.

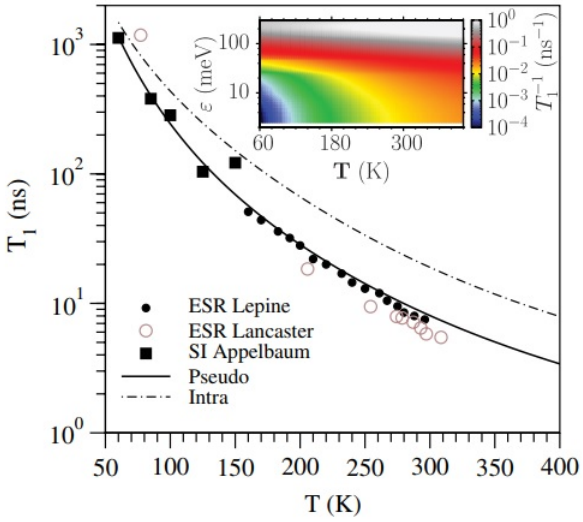

Figure 2.5: Spin Relaxation time in Si as a function of temperature [7].

Impurity scattering becomes important in doped Si, which reduces the spin lifetimes vs undpoed Si. Figure 2.6 shows the spin lifetime for n-type (phosphorous doped) Si that were deduced by from ESR linewidths from Pifer [20] at 10K for various doping densities and for one doping density using Hanle measurements [21]. The

measured lifetimes are between 10ns to 200ns depending on the level of doping.

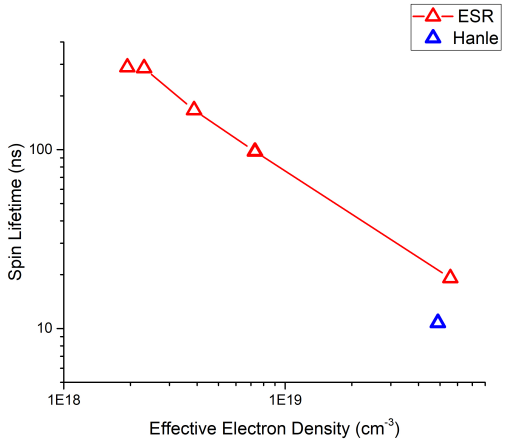

Figure 2.6: Spin lifetime measurements as a function of doping [22].

2.3 Selection Rules

The selection rules have been calculted by Cheng [23]. Figure 2.7 shows the selection rules for transitions from the valence band edge to the Z valley of the conduction band. The image shows possible transitions from the valence bands to the conduction band under σ^- light. The HH band is $\pm\frac{3}{2}$, the LH band is $\pm\frac{1}{2}$ in the upper row, and the SO band is $\pm\frac{1}{2}$ in the lower row. The arrows show which spin-polarization direction they will inject to and the numbers next to the arrows represent relative transition probabilities (e.g., 2 means 2x the probability as 1). The transverse acoustic (TA) and transverse optical (TO) phonons have equal probabilities for spin up and spin down in the LH band as well as the SO band, so they are not expected to contribute to the total DSP. For longitudinal acoustic (LA) phonons, there is an expected 50% DSP from the HH and LH bands. Adding the SO band will cause the DSP to go to 0%. A similar response is shown for longitudinal optical (LO) phonons in which a 50% DSP is expected for spin down with contributions from the HH and

LH bands with the DSP going to 0% with the inclusion of the SO band.

Figure 2.8 shows the X valley selection rules; the Y valley is identical to X so only the X valley is discussed. The LA phonons contribute equally to both spin directions for the HH, LH, and SO bands so no DSP is expected. The LO phonons contribute equally to each spin direction from the HH band. However, from the LH and SO bands the contributions are different for each, so the contributions won't add up to 0. The TA/TO phonons show the same thing.

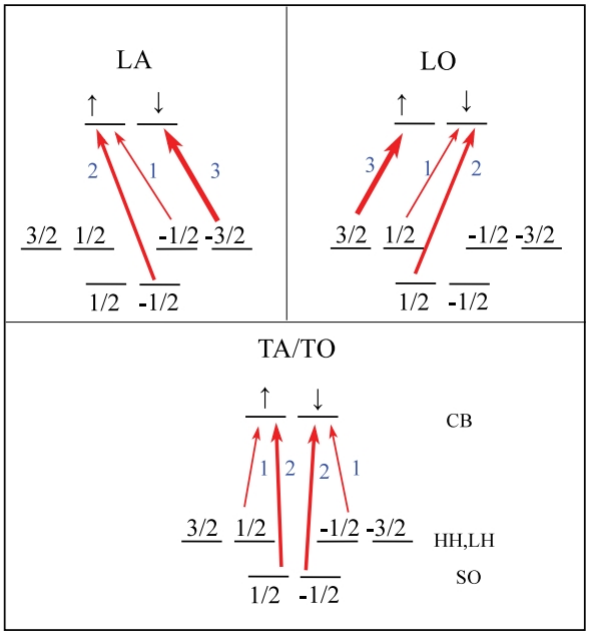

Figure 2.7: Selection Rules for the Z valley of Si [23].

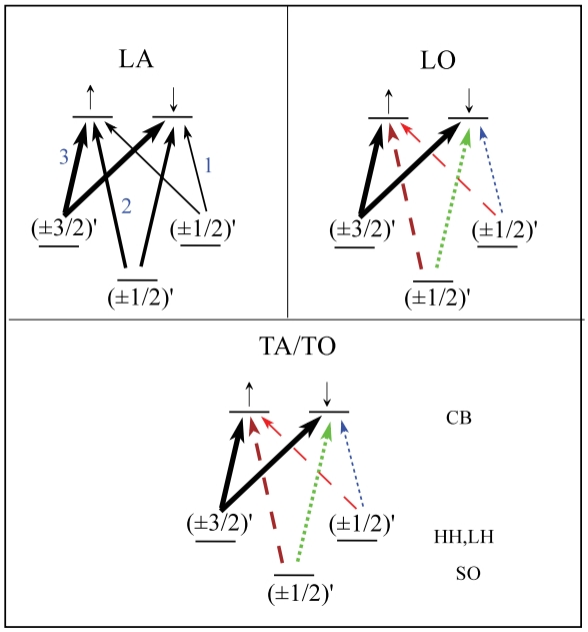

Figure 2.8: Selection rules for the X and Y valleys of Si [23].

2.4 Carrier and Spin Injection Rates

The total carrier injection rates are showin in Figure 2.9. The black lines were done with the full calculation while the red lines were done with band-edge approximations since these are the only bands that need to be considered at 4K. The calculations were done at 4K, at which only phonon emission is imortant. Figure 2.10 shows the contributions for each phonon branch. Inspecting the amplitude of these shows the largest contribution from phonon carriers are the TO phonons, followed by LO, then TA, and finally LA. The values increase along with the photon energy. It can also be seen that with the TO phonons, the band-edge approximations yield larger carrier injection rates than the full calculation. It's the opposite for the other phonons. There is also a trend in which the full caclulations become more important than the approximations as the contributions of the phonons become less important as the

difference between the calculations becomes greater. It should be noted that the current experiment only looks at T0 phonons, so the simplified calculation can be a good approximation for this experiment.

Figure 2.11 shows the calculations total spin injection rates at 4K. The rates increase with photon energy with the X valley dips negative and the Z valley goes positive, with the total being negative. With these calculations, the DSP can be calculated.

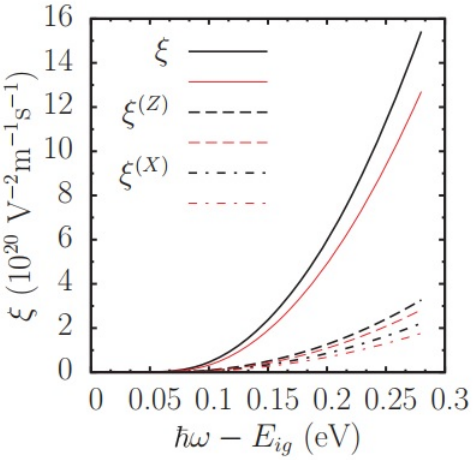

Figure 2.9: Calculation of carrier injection rates in Si. The x-axis is the energy level above the indirect bandgap [23].

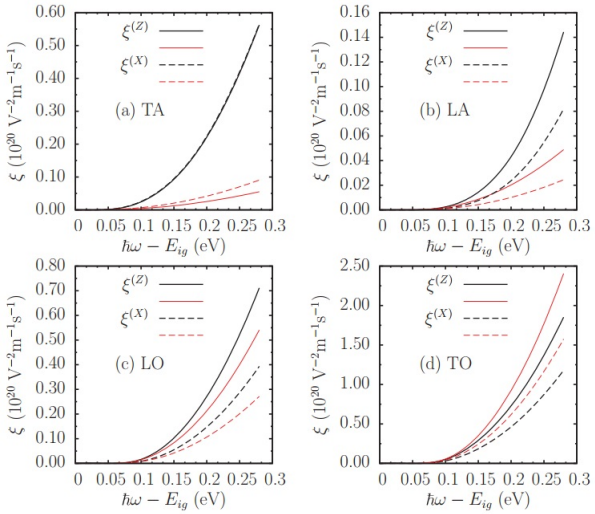

Figure 2.10: Calculations of the phonon contributions to the carrier injection rates [23].

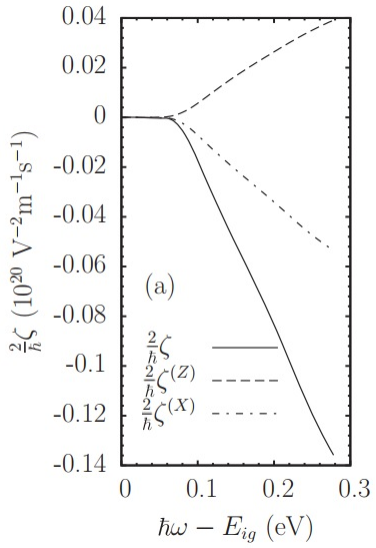

Figure 2.11: Calculation of total spin injection rates in Si [23]

2.5 DSP

The DSP is calculated by Cheng [23]:

$$DSP = \frac{\zeta}{\hbar\xi/2}, \quad DSP^{(I)}_{\{...\}} = \frac{\zeta^{(I)}_{\{...\}}}{\hbar\xi^{(I)}_{\{...\}}/2} \tag{2.1}$$

where ζ is the injection coefficient for spins and$\xi$is the injection coefficient for carriers. DSP is shown in Figure 2.12(a). The calculations were done at 4K with σ^- light. The X-axis is photon energy (in eV) above the indirect bandgap. The contributions from the Z valley differs from the X valley. The Y valley is identical to the X valley and wasn't computed. The solid line represents the total DSP while the two different dashed lines represent the DSP for the Z or X valley. There are three different energies that are noteworthy: $\hbar\omega_2 = 19meV$, $\hbar\omega_3 = 57meV$, and $\hbar\omega_4 = 90meV$. At $\hbar\omega_2$, the total DSP is -25% with 0% from the Z valley and -32% from the X valley. At $\hbar\omega_3$, the LA and LO phonons emissions are contributing, causing the DSP to significantly decrease. Here, the total DSP has been reduced to -1% with 5% from the Z valley and -5% from the X valley. At $\hbar\omega_4$, the total DSP has increased to -4% with -5% from the Z valley and -10% from the X valley. After this point, the DSP increases/decreases to 0 with increasing photon energy. From this, it can see the best location to search will be when only the TA phonons are emitted, between 19meV and 57meV above bandgap, closer to the 19meV threshold for the start of the TA phonon contribution.

Figure 2.12(b-c) shows the DSP the contribution that each phonon gives. At $\hbar\omega_2$, the contribution only comes from the TA phonon in the X valley, with the Z valley being 0. That means the only thing contributing to the DSP at this point is the TA phonons in the X valley. At $\hbar\omega_3$, all the phonons are turned on. In the Z valley, the LA and LO phonons add to 0, leaving 5% contribution from the TA phonons. In the X valley, the TA contribution has dropped to approximately -3% with the LA

and LO phonons giving about 1% and 5% respectively. The TO phonons give a large amount which causes the overall DSP in the X valley to drop from -5% to -10% at $\hbar\omega_4$. From this figure, it can be seen that the highest amount of DSP should be seen by exploring spin injection near where the first TA phonon turns on, $\hbar\omega_2$.

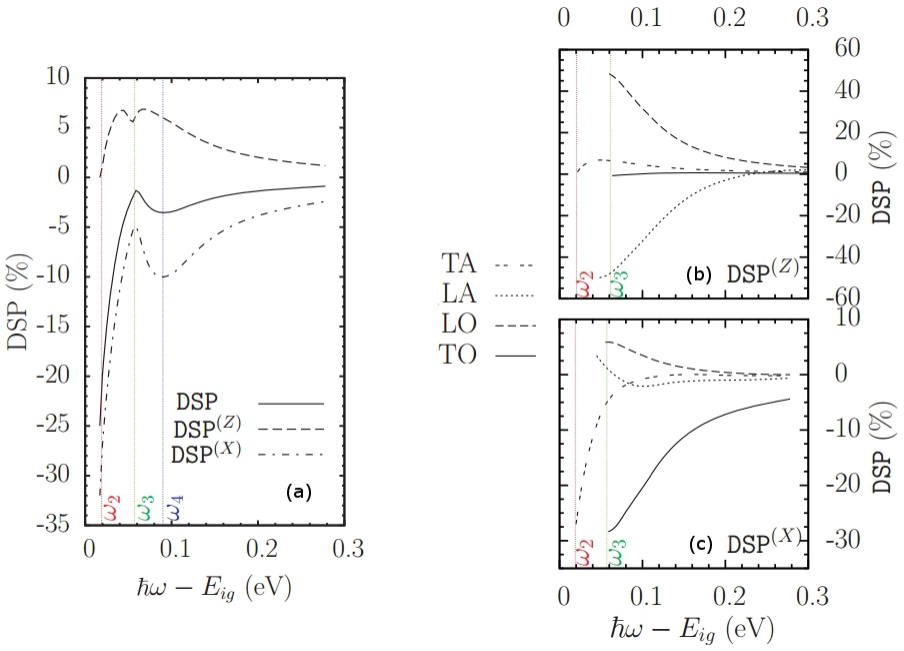

Figure 2.12: The calculated DSP at 4K. (a) shows the DSP for each valley. (b) shows the phonon contributions from the Z valleyx to the DSP. (c) shows the DSP contribution for the X valleys. [23].

Chapter 3

μSR

3.1 Muon Centers in Silicon

When an antimuon is implanted into Si, it can capture an electron or electrons to form a Mu center, which is a Mu atom inside a solid. These centers will cause alterations in the band structure of Si, allowing newly accessible energy levels allowed in the bandgap, as seen in Figure 3.1. There are two types of Mu centers in Si: paramagnetic, which is a antimuon and electron (Mu^0), and diamagnetic, which is either a bare antimuon (Mu^+) or an antimuon with two electrons (Mu^-). There are two types of Mu centers found in Si; the isotropic muonium center with a hyperfine parameter of $\omega_T = 2006.3MHz$ and the anomolous Mu center with the hyperfine parameters $A_\parallel = 92.6MHz$ and $A_\perp = 16.8MHz$ [24]. The isotropic Mu has been identified as the tetrahedral (T) site [25] and the bond-centered (BC) site that is located along the Si-Si bond on the <111> crystal axis [26].

Figure 3.1 shows that the energy line between Mu^+_{BC} and Mu^0_{BC} is located in the bandgap. The energy line between Mu^0_{BC} and Mu^-_{BC} lies outside the bandgap, in the conduction band. An examination of the T-site shows that ionization energy

required to turn Mu_T^0 to Mu_T^- lies within the valence band. Therefore, the Mu centers to consider inside Si are the Mu_{BC}^+, Mu_{BC}^0, Mu_T^0, and Mu_T^-. The Mu centers will eventually decay and give off a positron. Collection and analysis of these positrons allows for the determination of any spin polarization of the electrons that have been captured by the antimuons.

Figure 3.2 shows a model of what types of Mu centers to expect in Si. The solid lines represent states more prominent in p-type and intrinsic Si. In n-type Si, the Fermi level is lower resulting in the Mu_T^- state becoming imortant as shown by the dashed line. Since this experiment involves intrisnic and n-type Si, p-type Si won't be discussed.

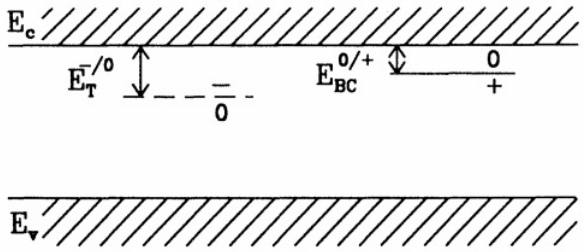

Figure 3.1: Energy levels within the bandgap [27]

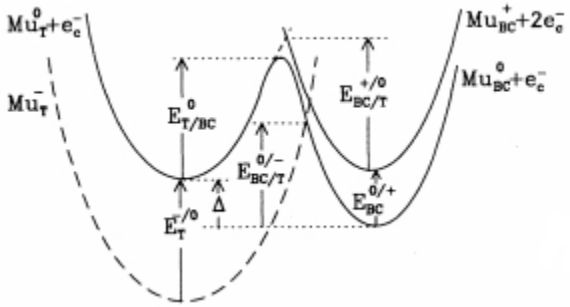

Figure 3.2: Adiabatic potential model for Mu centers in Si [27].

3.2 Muonium Transitions

The processes involved with the dynamics of Mu in Si under photoexcitation are given in Figure 3.3. The transition rates, Λ, dictate the transitions the Mu can take, whether it's a site transition, charge cycle, or spin exchange. The equations are listed in Table 3.1 where n is the net electron density, p is the net hole density, v_n is the electron thermal velocity, v_p is the hole thermal velocity, k_B is Boltzmann constant, T is the temperature, σ is the electron/hole capture cross section, E is the activation energy, and α is a prefactor frequency.

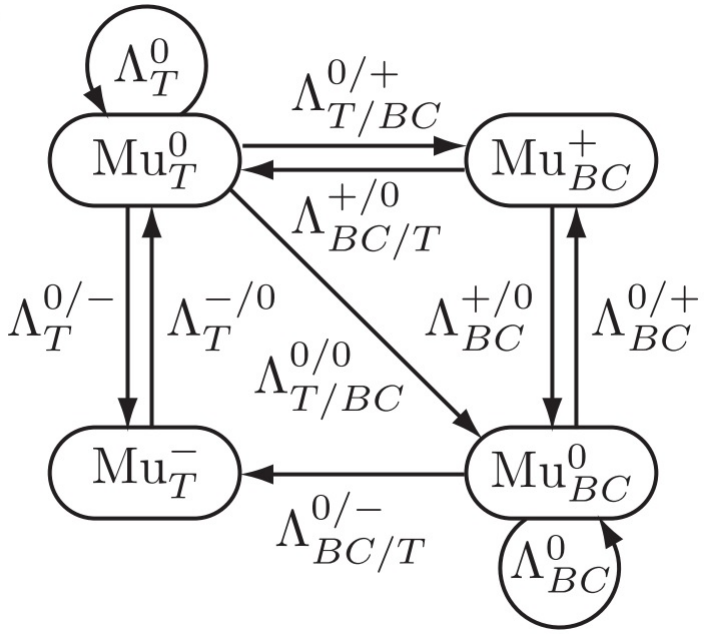

Figure 3.3: Four-state model of Mu in Si under photoexcitation [28]

At low temperatures, the site transitions drop many orders of magnitude. As an example, the transition rate for $\Lambda_{BC/T}^{0/-}$ from [28] is equal to 5.8MHz at T=291K while at T=20K, the rate is $1.4 * 10^{-81} MHz$. It is also worth noting that the Mu_{BC} cross sections for [28] are in the range of $\sim 10^{-8} - 10^{-12} cm^2$ while the range for the

Table 3.1: Equations for available Mu transitions. [28](see supplimental material)

BC0 RELAXATION	$\Lambda^{0}_{BC} = n v_n \sigma^{0}_{BC}$ $\Lambda^{0/+}_{BC} = \alpha^{0/+}_{BC} \exp\left[-E^{0/+}_{BC} / k_B T\right] + \mathrm{pv}_n \sigma^{0/+}_{BC}$ $\Lambda^{0/-}_{BC/T} = \mathrm{nv}_n \sigma^{0/-}_{BC/T} \exp\left[-E^{0/-}_{BC/T} / k_B T\right]$
BC+ RELAXATION	$\Lambda^{+/0}_{BC} = \mathrm{nv}_n \sigma^{+/0}_{BC}$ $\Lambda^{+/0}_{BC/T} = \mathrm{nv}_n \sigma^{+/0}_{BC/T} \exp\left[-E^{+/0}_{BC/T} / k_B T\right]$
T0 RELAXATION	$\Lambda^{0}_{T} = \mathrm{nv}_n \sigma^{0}_{T}$ $\Lambda^{0/0}_{T/BC} = \alpha^{0/0}_{T/BC} \exp\left[-E^{0/0}_{T/BC} / k_B T\right]$ $\Lambda^{0/+}_{T/BC} = \mathrm{pv}_p \sigma^{0/+}_{T/BC} \exp\left[-E^{0/+}_{BC/T} / k_B T\right]$ $\Lambda^{0/-}_{T} = n v_n \sigma^{0/-}_{T}$
T- RELAXATION	$\Lambda^{-/0}_{T} = \sigma^{-/0}_{T} \exp\left[-E^{-/0}_{T} / k_B T\right] + \mathrm{pv}_p \sigma^{-/0}_{T}$

same cross sections for [29] are in the range of $\sim 10^{-8} - 10^{-14} cm^2$, with the smaller cross sections from [28] being the charge cycling while the smaller from [29] being the spin exchange, so these cross sections are sample dependent and can't be used for our experiment. However, the sample used in [28] more closely resembles the n-type sample in this experiment while the sample in [29] is p-type so it is expected that the Mu_{BC} cross sections will more closely resemble the values from [28]. If this is the case, then the $\Lambda^{0/+}_{BC}$ and $\Lambda^{+/0}_{BC}$ transitions are expected to be larger than the hyperfine frequencies and won't cause any noticable depolarization of the antimuion spin. The in drop in these values due to temperature happens regaurdles of what the cross sections are, so site transitions can be ruled out at T=20K. To get these cross sections, and therefore the transition rates, a similar experiment will need to be carried out. What is known for sure is that any terms in the transition equations that have a temperature dependence can be neglected, which includes the site transitions as well as the initial term in the hole capture charge cycle processes.

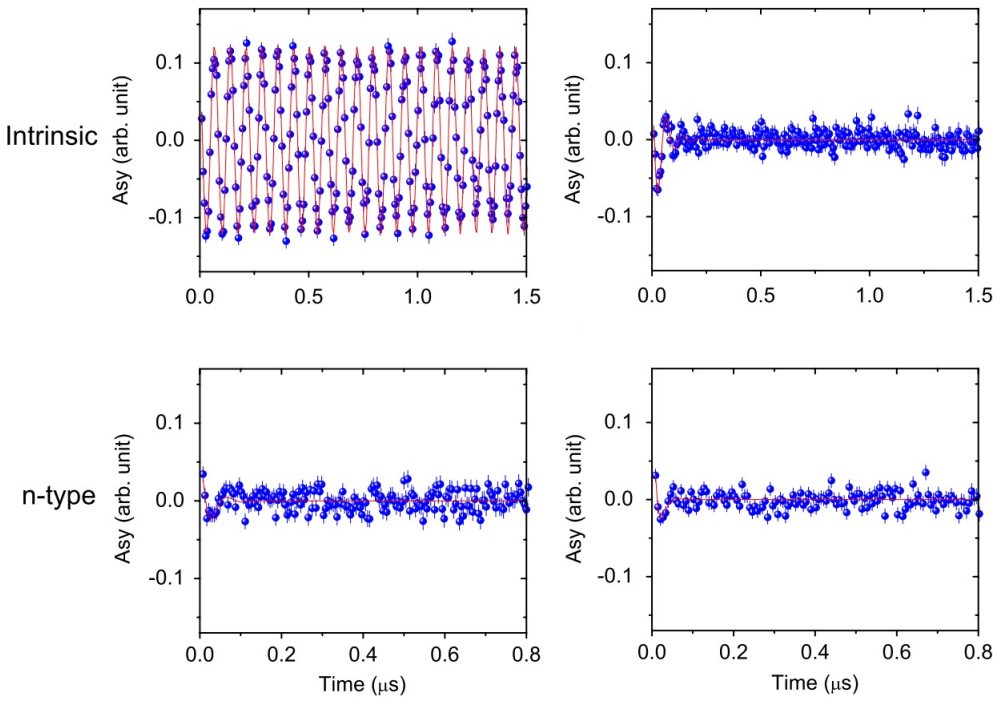

Figure 3.4: $TF - \mu SR$ measurements of p-type, intrinsic, and n-type Si samples in the dark and under illumination. Blue is data while red is a fit [30].

3.3 Isotropic Muonium

3.3.1 Eigenvalues

The Hamiltonian for isotropic Mu atom in an external magnetic (B) field is comprised of a hyperfine (1st) term and two Zeeman (2nd and 3rd) terms for the electron and antimuon respectively [31]:

$$H = \hbar\omega_{iso}\overrightarrow{S_e}.\overrightarrow{S_\mu} + g_e\mu_B B_{ext}S_e^{z'} + \hbar\gamma_\mu B_{ext}S_\mu^{z'} \tag{3.1}$$

where ω_{iso} is the isotropic hyperfine coupling constant, $\overrightarrow{S_e}$ and $\overrightarrow{S_\mu}$ are the electron and antimuon spin respectively, g_e is the spectroscopic splitting factor of the free electron,

μ_B is the Bohr magneton, B_{ext} is the applied external magnetic field, and γ_μ is the antimuon gyromagnetic ratio. The defined orientation of the applied magnetic field will be along the z'-axis where {x',y',z'} is the lab reference frame. Since the isotropic eigenfunctions are not dependent on direction, then an analytical solution is easily obtainable.

The basis states can be defined as the product of the spin of the electron and antimuon $|\Psi>=|S_e m_e>.|S_\mu m_\mu>$, where S is the spin quantum number ($\frac{1}{2}$ for both the electron and antimuon) and m is the secondary spin quantum number, which ranges from -S to S. Since S is the same for both, it's customary to leave S out and write the basis state as $|m_\mu m_e>$. I will also be referring to the basis states by the spin of the particles. So, writing the basis states out:

$$|1>=|\frac{1}{2},\frac{1}{2}>=|\uparrow\uparrow>$$

$$|2>=|-\frac{1}{2},\frac{1}{2}>,|\downarrow\uparrow>$$

$$|3>=|\frac{1}{2},-\frac{1}{2}>=|\uparrow\downarrow>$$

$$|4>=|-\frac{1}{2},-\frac{1}{2}>=|\downarrow\downarrow>$$

The eigensystem can be written in a 4x4 matrix yielding:

$$\frac{\hbar\omega_{iso}}{4}\begin{pmatrix} 1+2\chi_B d_\gamma & 0 & 0 & 0 \\ 0 & -1+2\chi_B d_\gamma & 0 & 0 \\ 0 & 0 & -1-2\chi_B d_\gamma & 0 \\ 0 & 0 & 0 & 1-2\chi_B d_\gamma \end{pmatrix}\begin{pmatrix} |1> \\ |2> \\ |3> \\ |4> \end{pmatrix}=E\begin{pmatrix} |1> \\ |2> \\ |3> \\ |4> \end{pmatrix}$$

where $\chi_b$is the reduced magnetic field $\chi_b = \frac{B_{ext}}{B_{iso}}$, $B_{iso} = \frac{\omega_{iso}}{-\gamma_e+\gamma_\mu}$, γ_e being the electron gyromagnetic ratio, and $d_\gamma = \frac{-\gamma_e-\gamma_\mu}{-\gamma_e+\gamma_\mu}$. The solutions are:

$$E_1 = \frac{\hbar\omega_{iso}}{4}(1+2\chi_b d_\gamma) \qquad |\Psi_1>=|1> \tag{3.2}$$

$$E_2 = \frac{\hbar\omega_{iso}}{4}(1-2\chi_b d_\gamma) \qquad |\Psi_2>=\frac{1}{\sqrt{2}}(\sqrt{1+\frac{\chi_b}{\sqrt{1+\chi_b^2}}}|2>+\sqrt{1-\frac{\chi_b}{\sqrt{1+\chi_b^2}}}|3>) \tag{3.3}$$

$$E_3 = \frac{\hbar\omega_{iso}}{4}(-1+2\sqrt{1+\chi_b^2}) \qquad |\Psi_3>=|4> \tag{3.4}$$

$$E_4 = \frac{\hbar\omega_{iso}}{4}(-1-2\sqrt{1+\chi_b^2}) \qquad |\Psi_4>=\frac{1}{\sqrt{2}}(\sqrt{1-\frac{\chi_b}{\sqrt{1+\chi_b^2}}}|2>-\sqrt{1+\frac{\chi_b}{\sqrt{1+\chi_b^2}}}|3>) \tag{3.5}$$

Plotting the eigenvalues and using $d_\gamma = 0.99037$ is shown in Figure 3.5. Looking at the basis states, we can see that there are two eigenfunctions that have the forms $|\uparrow\uparrow>$ and$|\downarrow\downarrow>$ while the other two eigenfunctions are comprised of a superposition of the other two basis states, $|\downarrow\uparrow>$ and $|\uparrow\downarrow>$, in which the probability of being in one state or the other is dependent on the applied B-field. If the applied B-field is 0, then the probability of being in one state vs the other is equal.

Another method for retrieving the eigenvalues is by the use of a software program called QUANTUM [32] that is written by James Lord for MANTID [33]. QUANTUM is a simulator written to be used in the MANTID program that allows for the calculations of the time evolution of antimuon spin. One feature that is built into QUANTUM is the calulation of the Breit-Rabi diagrams. The table setup for QUANTUM that yields the eigenvalues for the isotropic Mu is shown in Table 3.2. The solution is shown in Figure 3.6.

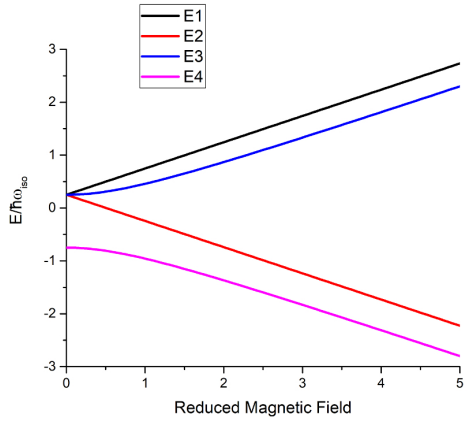

Figure 3.5: The Breit-Rabi diagram for the isotropic Mu

Table 3.2: Quantum Setup for solving for the the Mu_T^0

	Code[Y]	Value[Y]
1	spins	Mu,e
2	a(Mu)	2000
3	measure	breitrabi
4	lf	0,0,1
5	loop0par	bmagGauss
6	loop0range	-5000,5000,1001

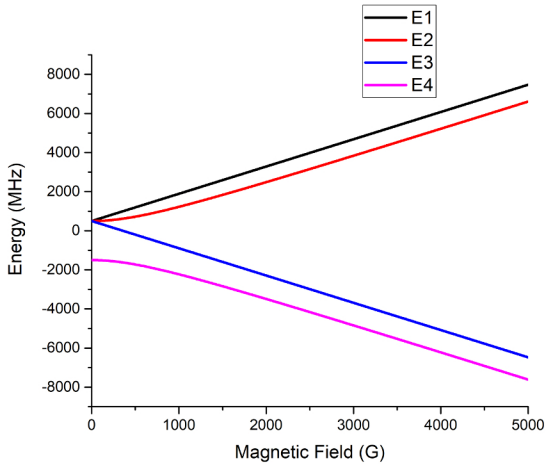

Figure 3.6: Breit-Rabi diagram for the Mu_T^0 solved through QUANTUM

3.4 Anisotropic Muonium

3.4.1 Eigenvalues

The Hamiltonian for the anisotropic Mu atom comprises three terms similar to the isotropic Hamiltonian. However, the first term, which defines the hyperfine coupling, now contains a tensor term, $\overrightarrow{A}$, instead of a constant ω_{iso} [31]:

$$H = \hbar \overrightarrow{S_e}.\overrightarrow{A}.\overrightarrow{S_\mu} + g_e \mu_B B_{ext} S_e^Z + \hbar \gamma_\mu B_{ext} S_\mu^Z \tag{3.6}$$

As with the isotropic Mu example, the magnetic field here is applied along the z'-axis of the lab reference frame {x',y',z'}. The crystal axis reference frame is defined as {x,y,z} where the <100> axis is along the z'-axis. Since the Mu is anisotropic, both the direction of the external B-field with respect to the crystal lattice, as well as the axis of symmetry for the Mu <111>, are important. The anisotropic Mu centers (BC) in Si are also close enough to the Si atoms along the bonds that they are placed on that the nuclear hyperfine interaction also needs to be considered. This requires the addition of the nuclear hyperfine interaction term to the Hamiltonian, which is of the form:

$$H_{NHF} = \hbar \sum \overrightarrow{S_N}.\overrightarrow{A_N}.\overrightarrow{S_e} - \sum g_N \mu_B B_{ext} S_N^Z \tag{3.7}$$

The solution to the eigenvalues can also be retrieved through QUANTUM. The settings in QUANTUM are shown on Table 3.3 and the Breit-Rabi diagram is shown on Figure 3.7.

Table 3.3: QUANTUM Setup for the Breit-Rabi diagram of anisotropic Mu in Si

	Code[Y]	Value[Y]
1	spins	Mu,e
2	a(Mu)	-67,51,1,1,1
3	measure	breitrabi
4	lf	0,0,1
5	bmagGauss	200
6	loop0par	bmagGauss
7	loop0range	-5000,5000,401

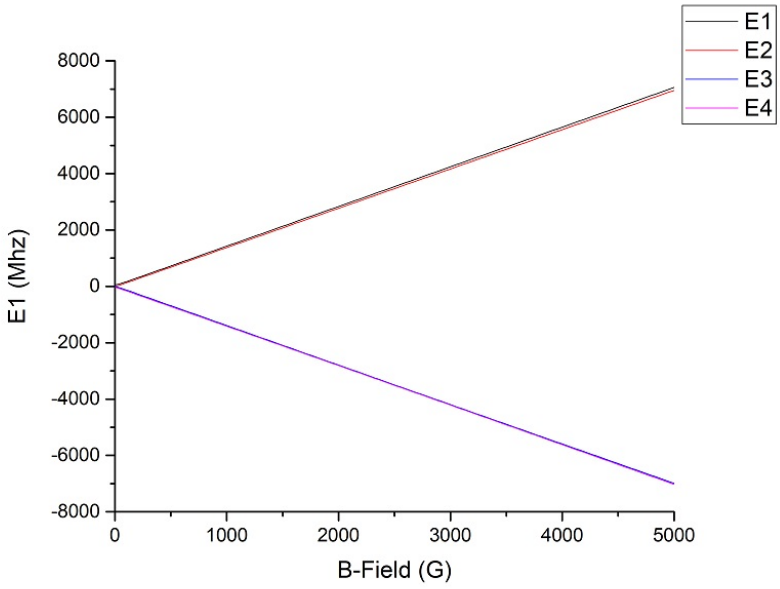

Figure 3.7: The Breit-Rabi diagram of anisotropic Mu in Si

Chapter 4

Experiment Setup

4.1 ISIS Muon Beam

The ISIS Pulsed Muon Facility at the Rutheford Appleton Labratory in England produces surface antimuons by the use of a synchrotron that creates a double pulse of 800 MeV protons at 50Hz that are 100ns width with a pulse separation of 230ns. The pulses of protons are extracted via an Extraction Kicker and are sent into a graphite production target to create pions. The two ways the pions can be formed are:

$$p^+ + p^+ \rightarrow p^+ + n + \pi^+$$

$$p^+ + n \rightarrow \pi^+ + n + n$$

where p^+ are the protons, n are the neutrons, and π^+ are pions. The pions have a lifetime of 23ns and decay to give antimuons that are 100% spin polarized opposite to the momentum (in the rest frame of the pion).

The pion decay can happen either within or outside the target material. The pions that decay close to the surface of the target can allow the antimuon to escape and be collected into a beam. These antimuons will all have the same polarization

causing the beam to be 100% spin polarized in the opposite direction of the beam propagation direction. An electrostatic kicker is then used to divert one of the pulses away to remove it. The final antimuon pulse that arrives at the target at the High Field (HiFi) spectrometer [34] will have a full width at half maximum (FWHM) of 70ns every 20ms.

4.2 High Field Spectrometer Experimental Setup

The experiment was conducted at the Rutherford Appleton Laboratory's ISIS Muon Facility. The detector used is the HiFi spectrometer (shown in Figure 4.1). This detector has small field coils that will provide up to a 400G magnetic field as well as high field coils that will provide magnetic fields up to 5T, both coils can apply the field in directions both parallel and anti-parallel to the antimuon spin. A transverse magnetic field of up to 150G can also be applied as well. It should be noted that the small fields are applied in opposite directions as the large fields in the longitudal direction, so a field of B=-50G is in the same direction as a field of B=+2500G.

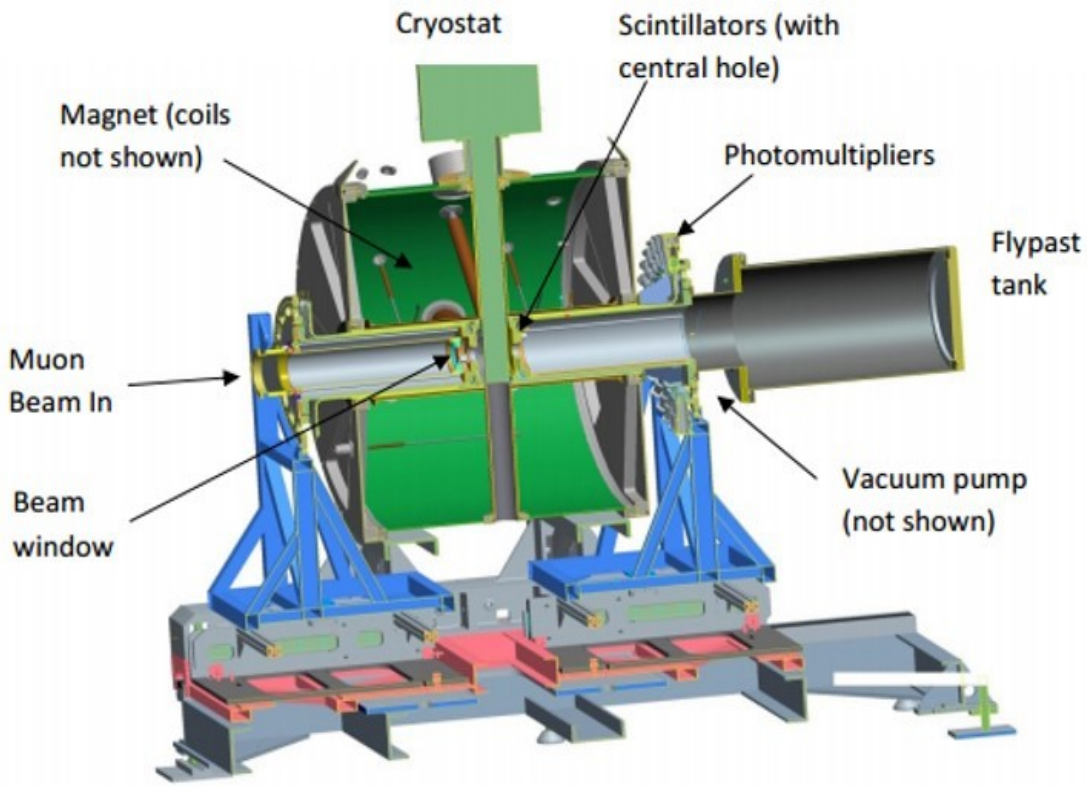

Figure 4.1: View of HiFi instruiment

The magnets used are superconducting, which means there are remnant fields still at the sample when the current to the magnets is turned off. To compensate for these fields in order to achieve a 0-field sample environment, there are two groups of three perpendicular Hall probes fitted on the same side of the beam line before and after the sample location. The field is measured at both locations and then using the equation:

$$\overrightarrow{B} = B_1\hat{z} + B_3((2z^2 - x^2 - y^2)\hat{z} - 2xz\hat{x} - 2yz\hat{y}) \tag{4.1}$$

the field that's expected at the sample location can be calculated. With this, then field at the sample can be set to 0.

Figure 4.2 shows the longitudal μSR setup employed. The antimuon beam enters and passes a detector that starts the t=0 timer for the experiment. The antimuon beam passes through an opening in the center of the detector and is stopped in the sample. The two detectors are split up into 64 detectors (32 in front and 32 in back, as shown in Figure 4.3). The laser passes through the backward detector and hits the sample from the other side at a variable time ,t_l, after the antimuon beam passes the t=0 detector. The antimuons decay and give off positrons whose direction of propagation is preferential to the antimuon spin direction at the time of decay.

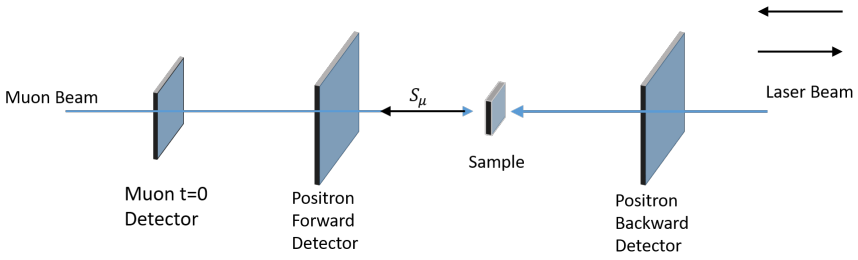

Figure 4.2: Configuration of sample enviroment.

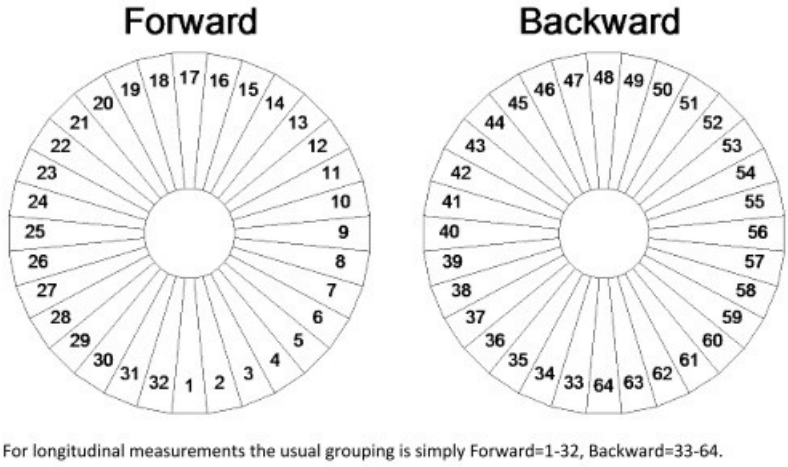

Figure 4.3: Positron detector configuration

The antimuon beam position and size are dependent on the magnetic field. As the

field is increased, the beam position and shape will change with focus points at both 2.5T and 4T. This experiment takes place entirely between 0T and 0.5T (5,000G). The beam is not focused here. Here, the beam starts off taller than it is wide. When the B-field is increased, the height of the beam drops off while the width slightly increases. The position of the beam between 0 and 1T was found to move around a spiral of 180°. However, this is compensated by steering magnets upstream. The height of the beam between 0-0.5T goes from around 1.26cm to 0.76cm while the width goes from around 0.96cm to 0.97cm.

Due to the presence of a magnetic field, the positrons will travel in a helical path with a radius proportional to the magnetic field. With the positrons having a distribution of energies up to 52.83 MeV, the maximum radius at 5T will be 3.5cm. A consequence to this travel path is that when the positron hits the edge of one of the detectors, the positron can move through to another detector and be counted twice. To prevent double counts, the number of detectors can be reduced. However, to accommodate high count rates, multiple detectors are required. The number of detectors for each front/back setup was chosen to balance the number of count rates possible while keeping double counts at a minimum.

When the positrons hit the detector plates, which are scintillators that are connected to light guides, they absorb the positron and emit a photon. The photon then travels through the light guide to a photomultiplier tube (PMT). From there, the signal from the PMT is put into a discriminator module to determine if the signal comes from the positron. The number of counts are put in bins of 16ns and stored in the computers using the Nexus file format. The files are broken up into approximately 20 million events (antimuon pulses) per file.

4.3 Sample Preparation

The sample needs to be cooled down uniformly to around 20K and be mounted in a strain-free configuration. Since the sample thicknesses are $300\mu m$ for the n-type and $500\mu m$ for the intrinsic, mechanical strain can be an issue. For this reason, the sample can't be affixed to a metal surface since that surface will have a different thermal expansion coefficient than the sample which will result in the sample being strained. The details of the two samples used are listed in Table 4.1.

Table 4.1: Sample properties of the Si wafers used in the experiment

SAMPLE	AXIS	DOPANT	WIDTH(μm)	TYPE	RESISTIVITY($\Omega . cm$)
N-TYPE	[100]	P	300	N	5-15
INTRINSIC	[100]		500	Intrinsic	10,000

The sample cell , as shown in Figures 4.4, 4.5, and 4.6, is constructed of aluminum with a 38.1mm diameter fused silica window for the laser side and a 57.8mm diameter titanium window for the antimuon side. There is a 30mm hole that allows the laser to pass through the sample holder to where the sample is located. The sample cell can hold samples up to 50.8mm in diameter and up to 3mm thick. The Si sample is placed in the sample cell through the antimuon window side. Then, a 1mm thick indium wire is placed in a channel around the sample. The antimuon window is placed and a retaining ring is placed over the antimuon window. There are a total of 16 screws that hold the antimuon retaining ring in and 12 screws that hold the laser side retaining ring in. The laser window is sealed with a polytetraflouroethylene (PTFE) o-ring and is never opened to preserve the seal.

The sample cell is placed into a helium glove box when sealed so it can easily be filled with helium gas when sealing. The helium gas in the cell is used for heat exchange to keep the sample uniformly cool. Aluminum degraders are then affixed to

the antimuon window side to allow for the antimuon pulse implantation depth to be controlled. The sample cell is then mounted on the closed cycle refrigerator (CCR). To ensure that the sample stays flat against the sample cell interior and doesn't tilt back towards the antimuon window, a small dab of Apiezon L vacuum grease is used at the top of the Si wafer, outside of the location of the antimuon and laser beam interactions. Not only does this keep the sample from tilting back against the antimuon window, it is also a strain-free style of mounting. Since the sample size in this experiment are 50.8mm in diameter, the wafers fit snugly in the location where the sample is placed. Proper alignment of the sample in the sample cell is important since it defines the alignment of the crystal axis of the Si to the applied magnetic field.

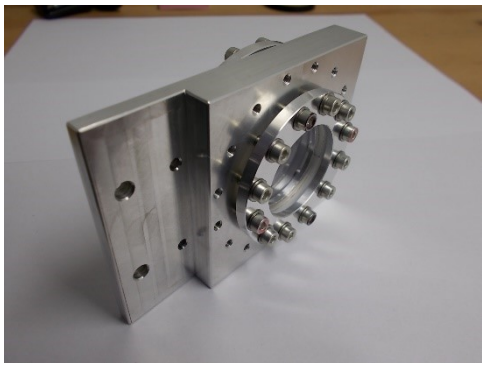

Figure 4.4: Sample Cell photo

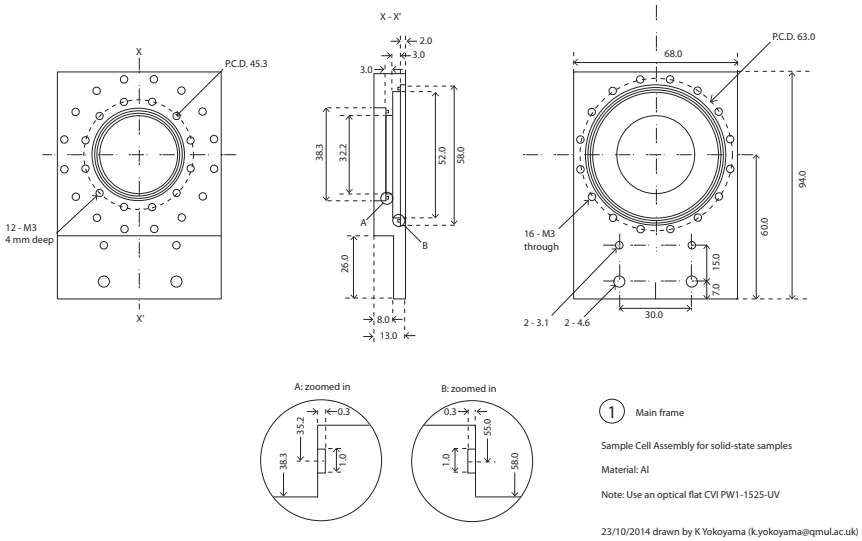

Figure 4.5: Sample Cell Diagram

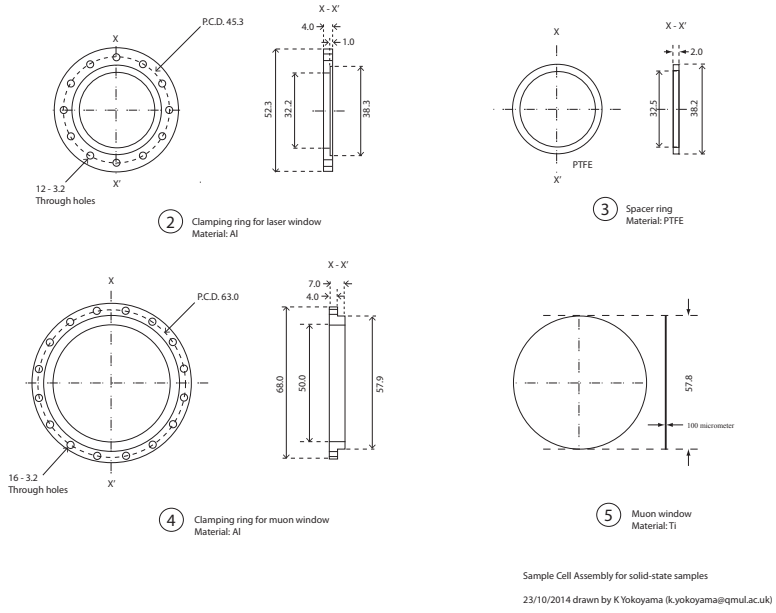

Figure 4.6: Sample Cell Parts

4.4 High Field Spectrometer Laser Setup

The laser used is a custom made Litron Lasers LTD. Q-switched neodymium-doped yttrium aluminum garnet (ND:YAG) laser with an included optical parametric oscillator (OPO). The laser system consists of two boxes on the table; the box for the laser oscillator and amplifier and the box for the harmonic generation (HG) crystals and OPO combination. The laser portion consists of the oscillator and two amplification stages that will deliver a maximum of 2.1J pulsed with a FHWM of 16ns at a repetition rate of 25Hz. This is fed into the HG portion of the second box which consists of second-, third-, fourth-, and fifth- HG crystals. This experiment uses the second and third HG crystals (SHG and THG respectively). The output from the SHG crystal will be a maximum of 1.2J at 532nm. The THG takes the 532nm and leftover 1064nm light and creates up to 415mJ of 355nm, which is then fed into the OPO. The OPO consists of two beta barium borate (BBO) crystals; the first which is used to generate the signal and idler outputs using a type II phase matching configuration while the second is used to compensate for any walk off. The signal can be tuned between 105 and 710nm while the idler can be tuned between 710 and 2400nm. The entire laser system is controlled via a laptop using software control, which can be controlled remotely from the user cabin. The wavelength is tuned by rotating the BBO crystals and reading the signal from a spectrometer and converting it to the idler using the equation:

$$\frac{1}{pump} = \frac{1}{signal} + \frac{1}{idler} \tag{4.2}$$

where the pump, signal, and idler are the wavelengths of the THG input and the signal and idler outputs.

Figure 4.8 is the laser table setup. Two dichroic mirrors are used between the first

attenuator to remove excess 532nm laser light that makes it past the optical parameter OPO. The cylindrical lenses are used to collimate the OPO beam. A second half wave plate is placed on the table and is used in combination with a polarizer in the Beam Transport System (BTS) as a secondary attenuator. The Interlock Shutter is a dual system consisting of both a manual and automatic shutter. The manual shutter is used to open and close the path from the laser cabin to the sample chamber with the automatic shutter taking over and closing when the interlock system is tripped. Univeral Serial Bus (USB) cameras are setup to read the positions of the half wave plate (HWP) attenuators which can be controlled remotely from the from the user cabin.

The BTS shown in Figure 4.9 connects the laser cabin to the Beam Entry Chamber (BEC) which is connected to the entrance port of the HiFi spectrometer. Mirror Box B contains a focusing lens and a beam sampler. The beam sampler is used to divert a small portion of the beam to a target along and a USB camera for alignment purposes. Mirror box D, also known as the BEC, is used to house polarizing optics that are required to be positioned just before the sample to ensure the correct polarization is reaching the sample. Due to the polarizing optics having a relatively small diameter, the beam is required to be reduced in size, so a beam reducer is put in before the polarization optics and a beam expander is placed after to bring the beam diameter back up to the proper size. There are three polarization optics that are mounted on an optical rail so they can be removed and put back in without the need for excess realignment. This also allows them to be aligned to the rail in the laser cabin since the BEC can't be open when the Interlock Shutter is open. The first optic on the rail is a linear polarizer that is set to allow only horizontal (P) polarization through. This, coupled with the second HWP in the laser cabin, allows for a secondary attenuator. The second optic is a Pockels cell which changes the P polarization by 90 degrees

(to vertical, or S) when voltage is applied; the beam will pass through without any polarization change when no voltage is applied. The final optic is a quarter wave plate (QWP) set at 45 degrees. This combination of optics allows for a final polarization of either left circularly polarized (LCP) or right circularly polarized (RCP) depending whether the Pockels cell has any voltage applied. There is also enough space between the polarization optics and the beam expander to place a power meter in temporarily to get a reading as close to the sample as possible. Since the Pockels cell is in mirror box D, the Pockels cell drive must also be present due to the length of the wires for the Pockels cell driver. Since the pockels cell switches high voltages around 3.4kV, interference in the electrical instruments in this box is entirely possible since the surface of the optical breadboard is metal. However, the interference is minimized by placing an insulating pad between the Pockels cell and optical breadboard. The voltage that is aplied to the Pockels cell is controlled remotely with a DC power supply in the user cabin and is linearly dependent on the wavelength of the laser. To set this quickly and efficiently throughout the experiment, several measurements were taken at the begninning of each run and fit, see Figure 4.7.

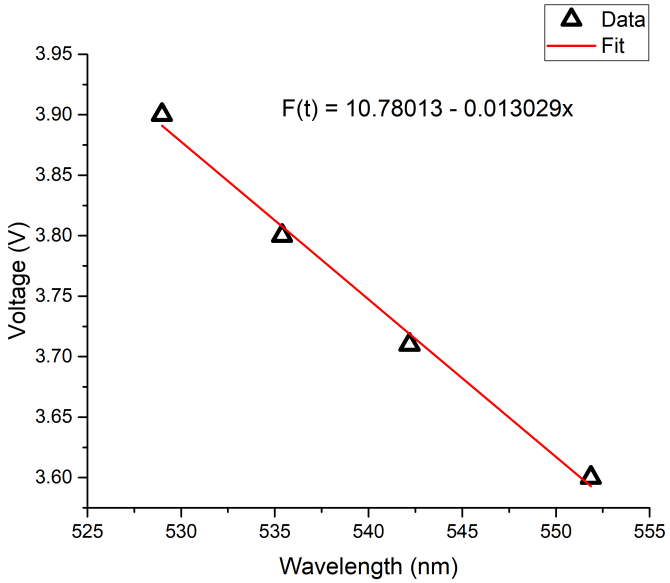

Figure 4.7: Pockels Cell Voltage Fit for May 2017

The beam is initially aligned using a class II 405nm alignment laser that is visible to the naked eye. This is used so the interlock system can be overridden to allow the mirror boxes to be open when the Interlock Shutter is open. On the laser table, there are two irises that are used to align the beam through the BTS and into the BEC. This will only bring the beam into the BEC and near the sample, but can't be used to align directly to the sample due to the distance from the interlock shutter to the sample being over 8 meters.

The beam is then further aligned along mirror box D at the height of the sample positioned inside the Hifi spectrometer. The first optic is a beam sampler to allow a USB camera to monitor the beam position which can be used for alignment purposes along with the other setup in mirror box B. The beam is initially aligned onto a target that is put into Hifi prior to the vacuum and cooling process. The beam is also aligned to a crosshair two different targets, one in mirror box B and another in mirror box D. Once the alignment laser is fully aligned, the main laser can be turned on and aligned,

first using the two irises on the table, to bring the beam to roughly the same position as the alignment laser. Then, final alignment can be made using the two targets that can be viewed by the USB cameras in the laser cabin. When considering the long travel distance between the two cameras (approximately 6 meters), the alignment to the sample is ensured with high confidence.

ISIS Target Station 1 is based on a pseudo 50Hz signal in a 5 pulse rotation, the first 4 pulses being actual antimuon pulses while the 5th is not an actual pulse. The Extraction Kicker generates a kicker signal when a pulse of protons is extracted. About $3.5\mu s$ later, the antimuons will arrive at the Hifi spectrometer. The laser system has two modes of operation: Mode 1, which uses the kicker signal generated from the protons that will create the current antimuon pulse and can be set anywhere from $3.0\mu s$ to 20ms from the time the antimuons arrive (t=0), and mode Mode 2, which uses the kicker signal from the previous proton pulse and can be set anywhere from -20 ms to $3.0\mu s$ from t=0. Since we are running the experiment at a time of approximately $0.5\mu s$ after the antimuon pulse arrives, we are using Mode 1. Mode 1 also has the benefit of the laser pulse jitter being much lower than Mode 2. There is an added delay of approximately $0.5\mu s$ due to the circuitry of the laser system. Also, it is worth noting that there are no more antimuons after $32\mu s$, so while the laser can be set to fire after this, there isn't much point in it.

The kicker signal is taken and sent to a Stanford DG655 digital delay box. This box then fires the laser's flashlamps at a time t1 after the received kicker signal. Then, it will fire the laser's Q switch at a time t2. Since firing the Q switch is the time when the laser pulse is shot, this is the delay that is set to coincide with the proper delay time in the experiment. To find the time the laser pulse arrives at the sample at a higher resolution, the "laser on" data is analyzed in detail to find where the initial drop in antimuon polarization occurs.

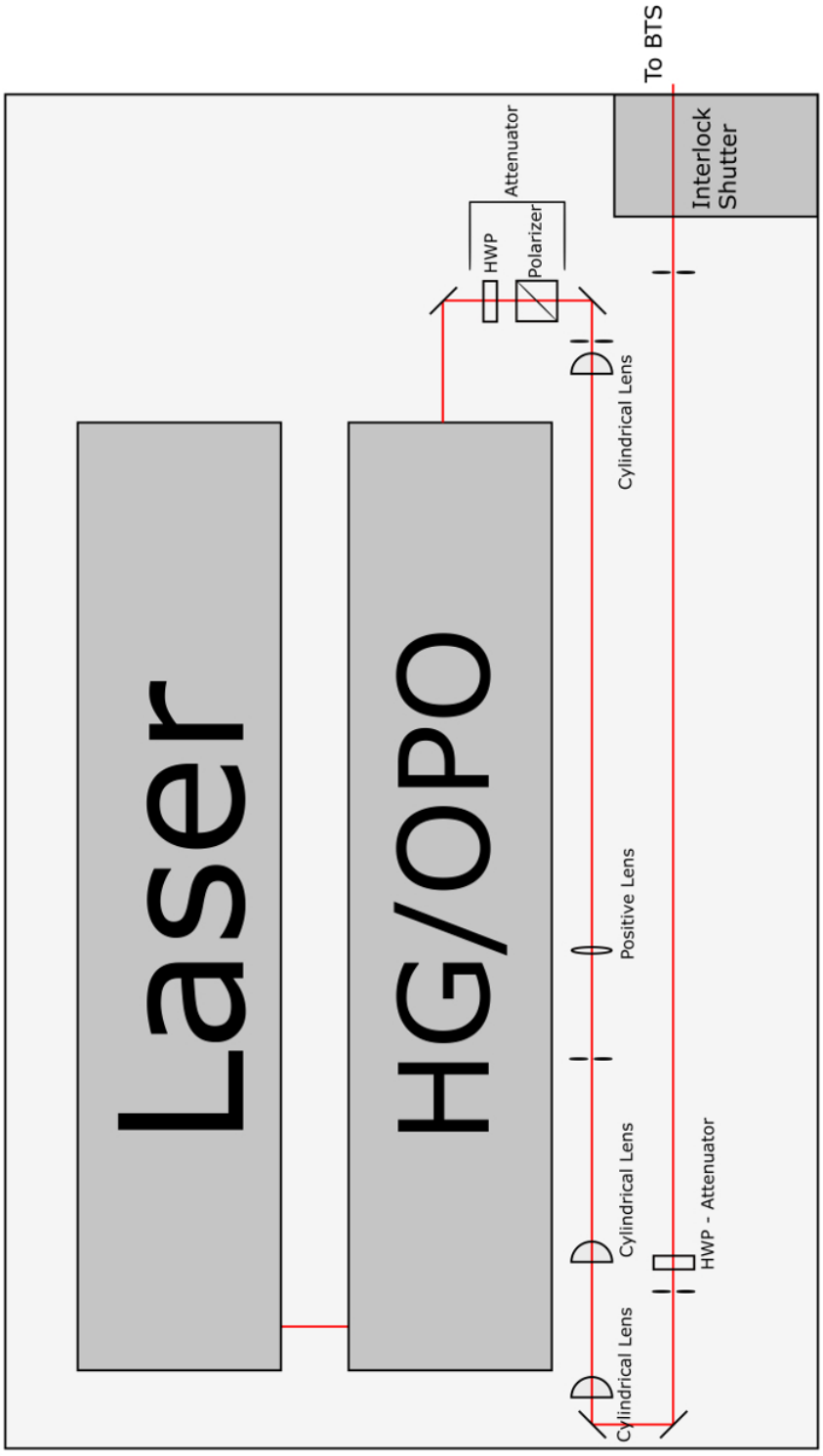

Figure 4.8: HiFi Laser Cabin Laser Setup

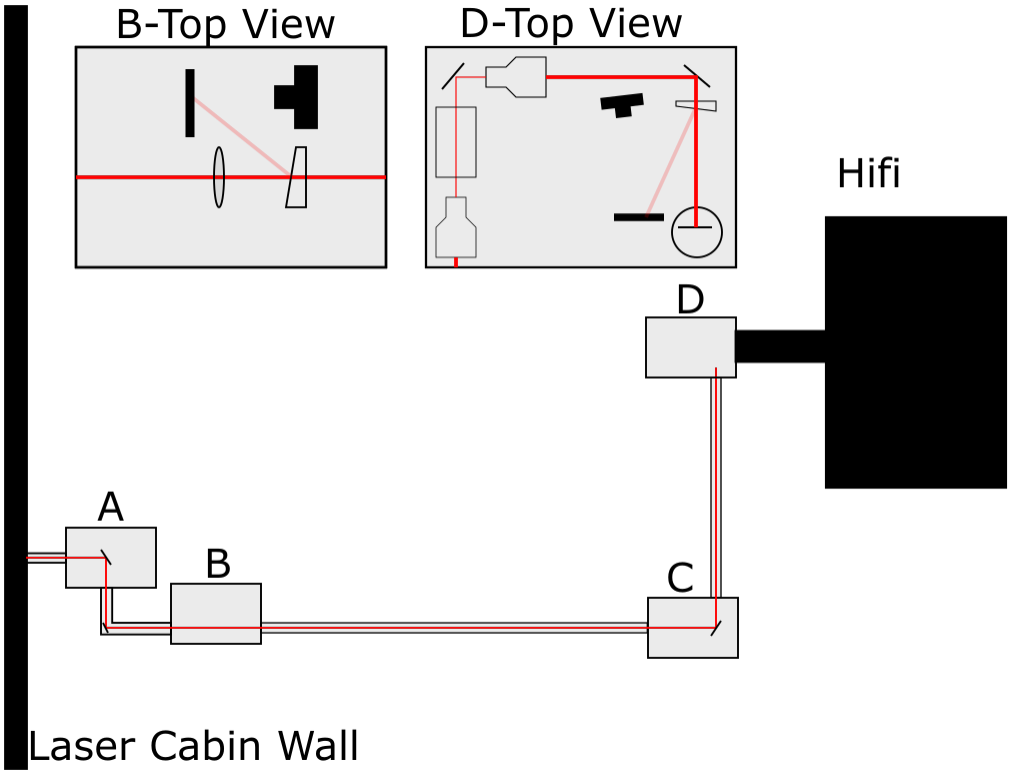

Figure 4.9: Beam Transport System that takes the laser from the laser cabin to the HiFi spectrometer

Chapter 5

Signal Analysis

Data for this experiment was accumulated over a total of four runs at the HIFI spectrometer. The first run went from July 14-19, 2015 (RB1510248). The second run went from February 18-24, 2016 (RB1610525). The third run went from December 2-7, 2016 (RB1620348). The fourth run was a continuation of the Dec. 2016 run and ran from May 4-8 2017 (RB1620348). The first two runs, July 2015 and Feb 2016, were done using an n-type Si sample while the last two, Dec 2016 and May 2017, were done with an intrinsic Si sample. The data taken at ISIS is taken at for $32\mu S$ per pulse in 16nS histogram bins, giving a total of 2048 bins per pulse. This can be plotted as a time spectrum and fit to the asymmetry function A[t].

5.1 Raw Data

The positrons decayed from the antimuons are detected at a rate of

$$N_{\pm}[t] = N_0 e^{-\frac{t}{\tau_\mu}}(1 \pm a_z P[t]) \tag{5.1}$$

in the forward (+) and backward (-) detectors. N_0gives the scale of the number of

positron counts, P(t) is the normalized polarization equation, $a_z$is the initial asymmetry, and τ_μ is the antimuon mean lifetime of 2.197μs. The data is captured in four periods: no laser, laser with Pockels cell off (positive helicity), no laser, laser with Pockels cell on (negative helicity). The two "no laser" periods, or "laser off" data, are added together and can be plotted as a function of counts vs time, as shown in Figure 5.1. Figure 5.2 shows a zoomed in portion of the graph to show the details at the start. The hump in the backward data around 0.1μs is an artifact due to excess positrons in the antimuon beam. To remove this, the data analyzed is taken after this bump. This anomaly is present in the data runs from July 2015 and Feb 2016, but is not present in the Dec 2016 run due to upgrades to the system.

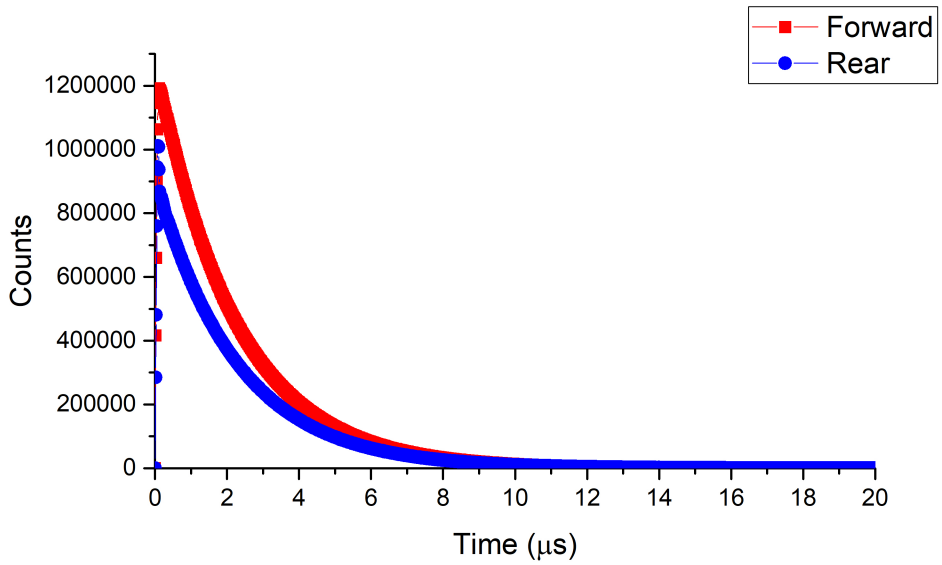

Figure 5.1: Time spectrum of positron decay.

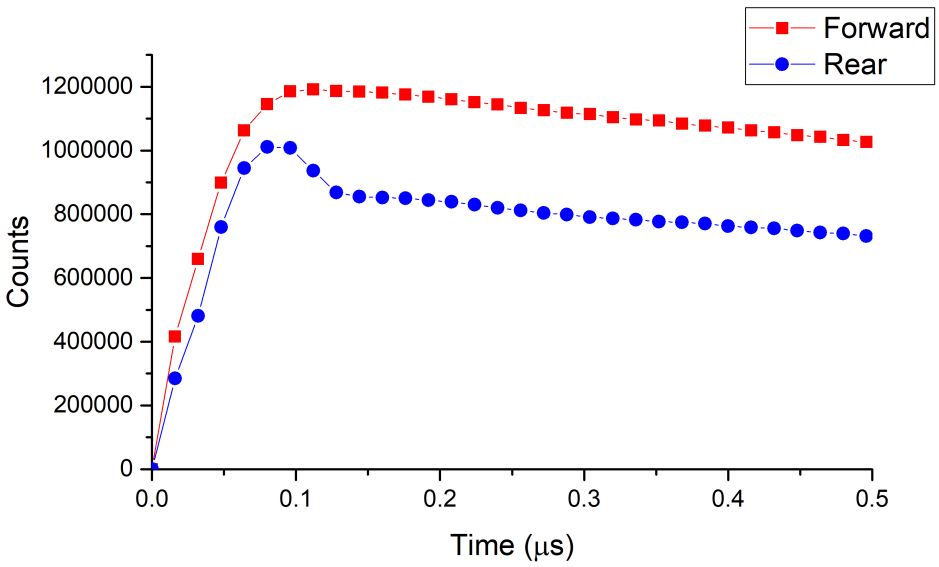

Figure 5.2: Zoomed in on the first half-microsecond of the positron decay time spectrum.

5.2 α Calculation

Due to the two detector plates having small differences from construction tolerances and changes in experimental variables, the two detectors may have an offset. To compensate for this offset, a balance coefficient (α) is introduced. α is calculated by viewing a data run at a small transverse field of 20G (TF20). At this field, the antimuon polarization is expected to oscillate around 0 asymmetry at a frequency of $1.394\frac{MHz}{G}$, so at 20G, the frequency is expected to be 27.9MHz and oscillate around 0 asymmetry. To estimate α, the data can be fitted to a cosine fit with an offset:

$$P[t] = A + BCos(\omega_{eff}t) \tag{5.2}$$

If the offset is not 0 asymmetry, then α is adjusted until the offset is equal to 0 asymmetry. The software WiMDA [35] has this feature built in which was used for

the values found below. It should be noted that this is an estimate of α since the actual offset is dependent on other factors which include the magnetic field, sample temperature, cycling of sample temperature, drift due to sample enviroment conditions, etc. However, the method of using a small transverse field data run to estimate α is a good approximation.

5.3 Time Integrated Data

The first type of data analysis is a time-integrated analysis in which A(t) is integrated over a period of time. The benefit of this type of analysis is that a total signal can be found from all the data. The downside is that any time -evolved information is lost. For the purposes of finding the total change in spin polarization, this type of analysis is suited. The degree of spin polarization can be found by:

$$DSP = \frac{A_{\sigma-} - A_{\sigma+}}{A_{\sigma-} + A_{\sigma+}} \tag{5.3}$$

where $A_{\sigma\pm}$are the time-integrated functions for A(t) for positive and negative helicities, respectively. The HiFi spectrometer collects data in bins of 16ns. These bins can be combined together in WiMDA with the use of the "bunch factor" feature. This feature combines the bins together into user-defined bunches. By defining the bunch factor to the maximum number of bins (2048), all the bins are put together into a single bin of data, effectively time-integrating the data.

5.4 Transverse Field Polarization Function

The polarization function for isotropic Mu in a transverse field is [31]:

$$P[t] = \frac{1}{4}[Cos(\omega_{12}t) + Cos(\omega_{14}t) + Cos(\omega_{34}t) + Cos(\omega_{23}t) + \frac{\chi_B}{\sqrt{1+\chi_B^2}}(Cos(\omega_{12}t) - Cos(\omega_{14}t) - Cos(\omega_{34}t) - Cos(\omega_{23}t))] \tag{5.4}$$

in which the angular frequencies are:

$$\omega_{12} = \frac{\omega_{iso}}{2}(1 + d_\gamma\chi_B - \sqrt{1+\chi_B^2}) \qquad \omega_{14} = \frac{\omega_{iso}}{2}(1 + d_\gamma\chi_B + \sqrt{1+\chi_B^2})$$
$$\omega_{23} = \frac{\omega_{iso}}{2}(-1 + d_\gamma\chi_B + \sqrt{1+\chi_B^2}) \qquad \omega_{34} = \frac{\omega_{iso}}{2}(1 - d_\gamma\chi_B + \sqrt{1+\chi_B^2})$$

with the ratio

$$d_\gamma = \frac{-\gamma_e - \gamma_\mu}{\gamma_e + \gamma_\mu}$$

where $\gamma_e$is the gyromagnetic ratio of a free electron and $\gamma_\mu$gyromagnetic ratio of an antimuon. The reduced magnetic field is

$$\chi_B = \frac{B_{ext}}{B_{iso}}$$

where B_{ext} is the applied external magnetic field and B_{iso} is a scaling field

$$B_{iso} = \frac{\omega_{iso}}{-\gamma_e + \gamma_\mu}$$

and the hyperfine coupling:

$$w_{iso} = -\frac{2\mu_0}{3}\frac{1}{\pi a_{Mu,0}^3}\gamma_e\hbar\gamma_\mu$$

with $\mu_0$the permeability of free space and $a_{Mu,0}$the ground-state radius of Mu. The data taken in all four runs have a small amount of transverse field data at low B-fields of 10G. Two simplifications can be made here:

1. If the applied external B-field is small, then the χ_B^2 term can be set to 0. Then, the frequencies are equal to:

$$\omega_{12} = \frac{\omega_{iso}}{2}(d_\gamma \chi_B) \qquad \omega_{14} = \frac{\omega_{iso}}{2}(2 + d_\gamma \chi_B)$$
$$\omega_{23} = \frac{\omega_{iso}}{2}(d_\gamma \chi_B) \qquad \omega_{34} = \frac{\omega_{iso}}{2}(2 - d_\gamma \chi_B)$$

2. The frequency ω_{iso} is too high to be detected on the HIFI spectrometer. This is because the spectrometer takes data in a time histogram with bins at 16ns, therefore any frequencies larger than roughly 62.5MHz will not be measurable, and since the frequency of ω_{iso} is between 2-4GHz, it's far too large to be detected. Therefore ω_{14} and ω_{24} can't be seen. The frequencies that will be detected are:

$$\omega_{12} = \omega_{23} = \omega_{eff}$$

This will reduce the polarization function to:

$$P[t] \simeq \frac{1}{2} Cos(\omega_{eff} t) \tag{5.5}$$

where $w_{eff} = \frac{\gamma_e}{4\pi} B$ and B is the applied magnetic field. This shows that in a small B-field, only half of the polarization amplitude is shown. This will not give any information on the Mu states, but can give definitive information on whether or not an antimuon signal is present. This information can also be used to calculate the detector balance coefficient α.

5.5 Longitudinal Polarization Function

5.5.1 Isotropic Muonium

The isotropic Mu repolarization curve can be found to be [31]:

$$P_{iso}[\chi_b] = \frac{1 + 2\chi_b^2}{2(1 + \chi_b^2)} \tag{5.6}$$

where χ_b is a reduced magnetic field $\chi_b = \frac{B_{ext}}{B_{iso}}$, in which $B_{iso} = 75mT$ for Mu_T^0 . With an applied B-field of $0mT$, this reduces to $\frac{1}{2}$. This can also be seen from the isotropic Mu mechanism. If the initial antimuon is spin $\uparrow$ and the electron spin has the chance to be 50% spin $\uparrow$ or 50% spin $\downarrow$. Therefore, the eigenstate can be 50% $|\uparrow\uparrow>$ ($|m_\mu m_e>$) or 50%$\uparrow\downarrow>$. The$\uparrow\downarrow>$ state yield 0% polarization since it alternates between $|\uparrow\downarrow>$ and $|\downarrow\uparrow>$, but the 50%$|\uparrow\uparrow>$will yield 50% polarization. In the high field limit, the B-field is so large that the hyperfine coupling is removed and the antimuons are all polarized in the direction of the magnetic field, reducing the above equation to 1. This plot shows what the initial polarization of the Mu_T^0 centers are in Si. It doesn't show the depolarization over time which happens due to other interactions, like interactions with the lattice and localized magnetic fields, that were ignored in the calculation of this function.

Figure 5.3 shows the repolarization curves for the Mu_T^0 for three different scenarios. These curves were obtained in QUANTUM. They show what the initial polarization of will be when an antimuon is implanted into the T-site and picks up an electron forming a Mu_T^0 . The red curve represents the case when the eigenstate is $|\uparrow\uparrow>$. The black curve shows the case when the eigenstate is $|\downarrow\downarrow>$. The blue curve is an average between them (the case of having 50% $|\uparrow\uparrow>$ and 50% $|\uparrow\downarrow>$).

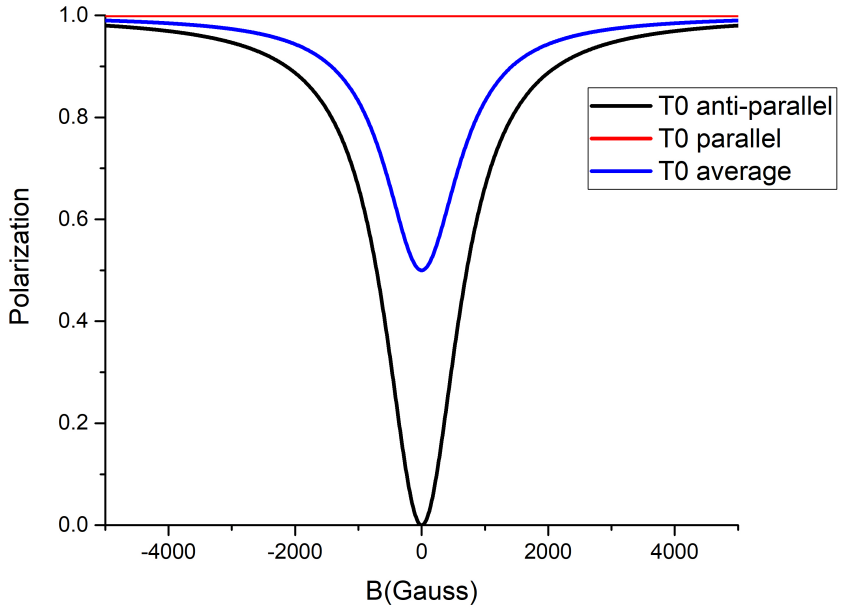

Figure 5.3: Repolarization Curve for Mu_T^0

The T centers in Si will depolarize over time due to other effects that haven't been accounted for with the repolarization curve, like lattice interactions. By time evolving the repolarization curve to take these depolarization effects, the expression for the Mu_T^0 centers can be described as [36]:

$$P_{T0}[t] \simeq P_{T0}[\chi_b] e^{-\lambda_{T0}(B)t} \tag{5.7}$$

$$\lambda_{T0}[\chi_n] = \frac{v_{T0}}{2(1+\chi_n^2)} \tag{5.8}$$

$$\chi_n[B] = \frac{2(\gamma_e + \gamma_\mu)B}{\omega_{T0}} \tag{5.9}$$

where $\omega_{T0}$is the Mu_T^0 hyperfine parameter and $v_{T0}$is the spin/charge exchange rate.

5.5.2 Anisotripic Muonium

The Mu^0_{BC} repolarization curve can be described by the equation [36]:

$$P_{ani}[B] = \frac{1}{8}\sum_{i=1}^{4}\{\frac{(\Omega_i - \gamma_\mu B)^2}{\Gamma_i^2 + (\Omega_i - \gamma_\mu B)^2} + \frac{(\Omega_i + \gamma_\mu B)^2}{\Gamma_i^2 + (\Omega_i + \gamma_\mu B)^2}\} \tag{5.10}$$

$$\Omega_i = \frac{1}{2}(\omega_\parallel Cos^2(\theta_i) + \omega_\perp Sin^2(\theta_i))$$

$$\Gamma_i = \frac{1}{2}(\omega_\parallel - \omega_\perp)Sin(\theta_i)Cos(\theta_i)$$

in which $\omega_\parallel$ and $\omega_\perp$ are the Mu^0_{BC} hyperfine parameters and θ_i is the angle between the applied magnetic field B and the BC axis of symmetry, crystal axis <111>, and the summation is over the four different <111> axes of Si. This curve can also be found through QUANTUM. Figure 5.4 shows the repolarization curves; the red curve represents the case when the electron and antimuon spin are both spin ↑, the black curve shows the case when the electron is spin ↓ and antimuon is spin ↑, and the blue curve has antimuon spin up and the elctron spin is 50% spin ↑ and 50% spin ↓. The ALC resonsance can be seen as the dip at B=2750G. This resonance effect is due to the interaction with the spin of the electron attached to the Mu center and the nuclear spin of the neighboring atoms.

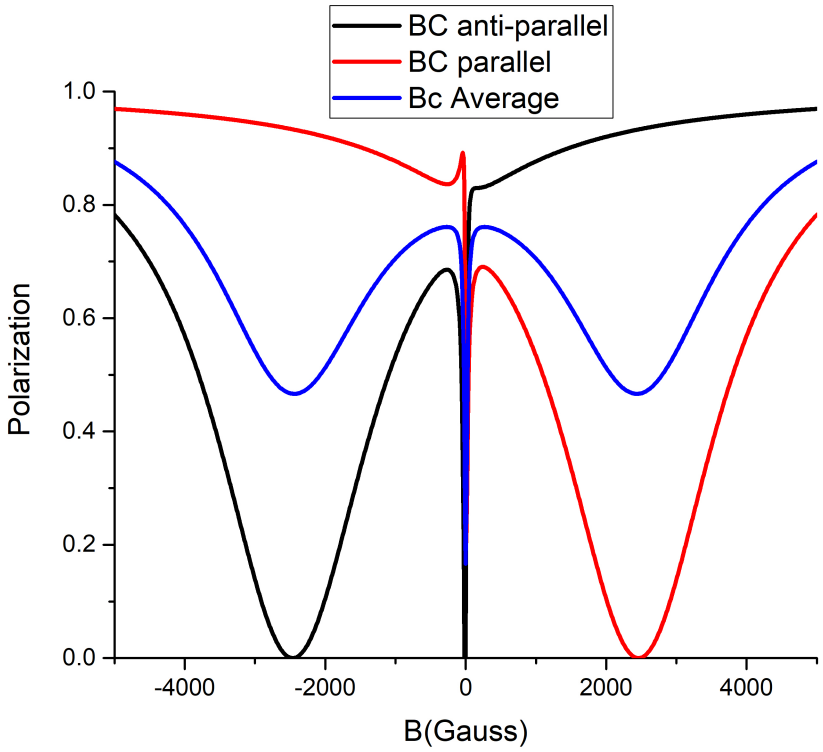

Figure 5.4: Repolarization curves for Mu^0_{BC}

The Mu^0_{BC} centers in Si also depolarize over time and take the form [36]:

$$P_{BC}[t] \simeq P_{ani}[B]e^{-\lambda_{BC}(B)t} \tag{5.11}$$

$$\lambda_{BC}[B] = v[1 - P_{ani}[B]] \tag{5.12}$$

5.5.3 Asymmetry

The raw data is then taken and the asymmetry is calculated by

$$A[t] = \frac{N_+(t) - \alpha N_-(t)}{N_+(t) + \alpha N_-(t)} \tag{5.13}$$

The asymmetry equation can be calculated for no laser on the sample (laser off), positive helicity, negative helicity, and the addition of the positive and negative helicity

to create "laser on" data. Plugging in the equation above yields:

$$A[t] = \frac{(1-\alpha) + a_z P(t)(1+\alpha)}{(1+\alpha) + a_z P(t)(1-\alpha)} \tag{5.14}$$

For longitudinal external B-fields with no laser applied, the asymmetry data can be fit to the function:

$$A[t] = A + Be^{-\gamma t} \tag{5.15}$$

where the initial asymmetry is defined as $A + B$ and the asymmetry decay rate is γ. For transverse B-fields with no laser applied, the asymmetry data can be fit to the function

$$A[t] = A + BCos(\omega_{eff} t) \tag{5.16}$$

5.6 Rate Equation for Positron Decay

Since the antimuons travel as a gaussian pulse, the positron decay can be described as:

$$\frac{\partial N_P[t]}{\partial t} = -\frac{N_P[t]}{\tau_\mu} + g[t] \tag{5.17}$$

where τ is the antimuon decay rate and $g[t]$ is a gaussian pulse:

$$g[t] = \frac{N_{Ptot}}{t_p\sqrt{\pi}} e^{-(\frac{t-t_m}{t_p})^2} \tag{5.18}$$

Plugging this in and solving:

$$N_P[t] = \frac{N_{Ptot}}{2} e^{(\frac{t_p}{2\tau})^2 - \frac{t-t_m}{\tau}} (Erf[\frac{t_p^2 - 2\tau_\mu(1-t_m)}{2\tau_\mu t_p}] - Erf[\frac{t_p^2 - 2\tau_\mu(t-t_m)}{2\tau_\mu t_p}] \tag{5.19}$$

where N_{Ptot} is the peak positron count, t_m is the time of antimuon implantation

(meaing t=0 is the time of the antimuon pulse passes the t=0 detector), and t_p is half of the antimuon pulse FWHM.

5.7 Rate Equations for Muonium

After examining the transition equations in Figure 3.1, a model for the muonium decay can be constructed. Assuming the simplest form, by only including the spin-exchange terms, the rate equations are constructed as follows:

5.7.1 Isotropic Muonium Mechanism

The isotropic Mu in Si reside at the T site. Examining the spin exchange, consider the case where the applied B-field is 0. The antimuons are implanted into the Si with the spin in the forward direction ($\uparrow$). Also consider that the unpolarized sample has 50% of the electrons with spin $\uparrow$ and 50% with spin $\uparrow$. This case was explained previously (see Section 5.5.1). The polarization of this case turns out to be $P = 50\%$. For the case when 100% of the electrons are spin $\uparrow$, the only state will be $|\uparrow\uparrow>$, meaning the polarization will be $P = 100$. For the case when 100% of the electrons are spin $\downarrow$, there will only be the superposition of $|\uparrow\downarrow>$ and $|\downarrow\uparrow>$, yielding a polarization $P = 0$. These values can be seen in Figure 5.3).

Now, set B=2750G. From the repolarization curves for T0 (see Figure 5.3), for 100% electron spin $\uparrow$ the polarization is 100%, for 100% electron spin $\downarrow$ the polarization is 96.9%, and for 50% electrons spin $\uparrow$ and $\downarrow$the polarization is 93.8%. When putting in 100% electron spin $\uparrow$, the only state made is $|\uparrow\uparrow>$, so the polarization made will be $P = 100$. For 100% electron spin $\downarrow$, the magnetic field causes the antimuon to want to stay in its spin position, so the states that are made are 96.9% $|\uparrow\downarrow>$ and 3.1% $|\downarrow\uparrow>$. Therefore, the polarization made is $P = 100\%(96.9\% - 3.1\%) = 93.8\%$For 50%

electrons spin $\uparrow$ and $\downarrow$, 50% are made with $|\uparrow\uparrow>$ and 50% are made with 96.9% $|\uparrow\downarrow>$ and 3.1% $|\downarrow\uparrow>$. Therefore, the polarization is $P = 50\%(100\%)+50\%(96.9\%-3.1\%) = 96.9\%$.

Now, consider what happens when the laser hits the sample with circularly polarized light. Since the polarization of the laser will be circularly polarized, the light will be either σ^+ or σ^-, meaning the photons are either spin $\uparrow$ or spin $\downarrow$. Once the spin is absorbed, the electrons are now $\frac{1+DSP}{2}$ $\uparrow$ and $\frac{1-DSP}{2}$ $\downarrow$. The laser comes around $0.75\mu s$ after the antimuons are implanted into the sample. The $Mu^0_{T\uparrow}$ loses an electron and captures an electron by: $\frac{1+DSP}{2}|\uparrow\uparrow>$delivers no change, $\frac{1-DSP}{2}|\uparrow\downarrow>$ delivers $96.9\%|\uparrow\downarrow> +3.1\% \downarrow\uparrow>$. The $Mu^0_{T\downarrow}$loses and electron and captures an electron by: $\frac{1+DSP}{2}|\downarrow\downarrow>$delivers no change, $\frac{1-DSP}{2}|\downarrow\uparrow>$ delivers $3.1\%|\uparrow\downarrow> +96.9\% \downarrow\uparrow>$.

The portions that yeild a change in the antimuon spin from both the $Mu^0_{T\uparrow}$ and $Mu^0_{T\uparrow}$ are the portions that have the 3.1% attached. To create the decay rate functions, these terms will subract from the decay rates. Since the term from $Mu^0_{T\uparrow}$ is converted to $Mu^0_{T\downarrow}$ and visa versa, detailed balance states that the term subtracted from $Mu^0_{T\uparrow}$ is added to $Mu^0_{T\downarrow}$as well as the term from $Mu^0_{T\downarrow}$is added to $Mu^0_{T\uparrow}$. Therefore, the decay rate equations can be written as:

$$\frac{d(N_{T0\uparrow}(t))}{dt} = 0.31k_{T0}n_e(t)(-\frac{1-DSP}{2}N_{T0\uparrow}(t) + \frac{1+DSP}{2}N_{T0\downarrow}) - \frac{1}{\tau}N_{To\uparrow} - \frac{\gamma}{2}(N_{T0\uparrow} - N_{T0\downarrow})$$

$$\frac{d(N_{T0\downarrow}(t))}{dt} = 0.31k_{T0}n_e(t)(\frac{1-DSP}{2}N_{T0\uparrow}(t) - \frac{1+DSP}{2}N_{T0\downarrow}) - \frac{1}{\tau}N_{T0\uparrow})$$
$$-\frac{\gamma}{2}(N_{T0\downarrow} - N_{T0\uparrow})$$

where

$$n_e(t) = \frac{n0_e}{1+\beta n0_e t}$$

with γ and τ added as decay rates for the phosphorous charge cycle (see Equation 6.1) and antimuon decays respectively. Taking the difference of these two equations:

$$\frac{d(dN_{T0}(t))}{dt} = -0.31k_{T0}n_e(t)(dN_{T0}(t) - DSP(sN_{T0}(t)) - (\gamma + \frac{1}{\tau})dN_{T0}(t) \quad (5.20)$$

The summation is:

$$\frac{d(sN_{T0}(t))}{dt} = -\frac{sN_{T0}(t)}{\tau}$$

Solving this equation yields

$$dN_T[t] = e^{\frac{(t-tl)+\gamma\tau(t-tl)}{\tau}}(dN0_{T0}(1+(t-tl)\beta n0_e)^{-\frac{0.031k_T}{\beta}} + (DSPe^{-\frac{\gamma}{\beta n0_e}}$$
$$k_T(-0.031DSPGamma[A](\gamma(tl-t-\frac{1}{\beta n0_e}))^{-\frac{0.031k_T}{\beta}} + 0.031Gamma[B]$$
$$(-\frac{\gamma}{\beta n0_e})^{-\frac{0.031k_T}{\beta}}(1-(t-tl)\beta n0_e)^{-\frac{0.031k_T}{\beta}})sN0_T)/\beta$$

where

$$Gamma[A] = Gamma[\frac{0.031k_T}{\beta}, \gamma(tl - t - \frac{1}{\beta n0_e})]$$
$$Gamma[B] = Gamma[\frac{0.031k_T}{\beta}, -\frac{\gamma}{\beta n0_e}]$$

5.7.2 Anisotropic Muonium Mechanism

The anisotropic Mu in Si reside on a bond between two Si atoms, called the BC site. If an external B-field is applied along the <100> (z) axis of the Si lattice, a resonance effect will be seen at an applied B-field of B=2750G. This resonance spin flipping is due to interactions with the Mu spin and the neighboring nuclear spin and has an effect of lowering the polarization of the Mu_{BC} centers. An effect of this resonance is that the eigenstates to behave differently than what they would elsewhere. The states can be written as:

$$|X\uparrow\!>\!:\!\rightarrow\uparrow\!>, |\downarrow\uparrow\!>, |\leftarrow\uparrow\!>, |\uparrow\uparrow\!> \tag{5.21}$$

$$|X\downarrow\!>\!:\!\rightarrow\downarrow\!>, |\downarrow\downarrow\!>, |\leftarrow\downarrow\!>, |\uparrow\downarrow\!> \tag{5.22}$$

$$|\uparrow\downarrow\!>$$

$$|\downarrow\downarrow\!>$$

where the Mu in the X-states are precessing around the x-axis.

The Mus will all be implanted into the sample with 100% spin $\uparrow$. If the electrons are all spin $\uparrow$, then all the electrons go to $|\uparrow\uparrow\!>$which precess in state $|X\uparrow\!>$. The amount in $|\uparrow\uparrow\!>$ and $|\downarrow\uparrow\!>$ depends on the B-field. Looking at Figure 5.4, for Mu spin $\uparrow$100% electron spin $\uparrow$, P=94.0%, for Mu spin $\uparrow$100% electron spin $\downarrow$, P=4.39%, and for Mu spin $\uparrow$50% electron spin $\uparrow$ and 50% electron spin $\downarrow$, P=49%.

When the laser hits, it will strip electrons off the Mus and they'll capture another electron. This process can be described as:

For $Mu^0_{BC\uparrow}$, it will capture an electron with spin $\uparrow$to form $\frac{1+DSP}{2}|\uparrow\uparrow>$. At the resonance of 2500G, it will be an equal amount of which precesses and be in each state at equal amounts. However, since the experiment was done at 2750G, there is a 4.39% polarization for $|\uparrow\uparrow>$. Therefore, states that form with $\frac{1+DSP}{2}|\uparrow\uparrow>$ will be 47.805% $|\downarrow\uparrow>$ and 52.195% $|\uparrow\uparrow>$. It can also capture an electron with spin $\downarrow$ to form $\frac{1-DSP}{2}|\uparrow\downarrow>$, which 94% goes to $|\downarrow\uparrow>$ and 6% goes to $|\downarrow\uparrow>, |\rightarrow\uparrow>, |\uparrow\uparrow>, |\leftarrow\uparrow>$ with 3% $|\downarrow\uparrow>$and 3% $|\uparrow\uparrow>$. For $Mu^0_{BC\downarrow}$, it will capture an electron with spin $\uparrow$to form $\frac{1+DSP}{2}|\downarrow\uparrow>$ which precesses with 47.805% $|\downarrow\uparrow>$ and 52.195% $|\uparrow\uparrow>$. It can also capture an electron with spin $\downarrow$ to form $\frac{1-DSP}{2}|\uparrow\downarrow>$, which 94% goes to $|\downarrow\downarrow>$ and 6% goes to $|\downarrow\downarrow>, |\rightarrow\downarrow>, |\uparrow\downarrow>, |\leftarrow\downarrow>$ with 3% $|\downarrow\uparrow>$and 3% $|\uparrow\uparrow>$. The decay rates can be writting by only the processes that change the Mu spin. The equations are:

$$\begin{aligned}\frac{d(N_{BC\uparrow}(t))}{dt} &= -k_{BC0}n_e(t)((\frac{1+DSP}{2}(52.195\%)N_{BC\uparrow} + \frac{1-DSP}{2}(3\%)N_{BC\uparrow}) \\ &+(\frac{1+DSP}{2}(52.195\%)N_{BC\downarrow} + \frac{1+DSP}{2}(3\%)N_{BC\downarrow})) - \frac{1}{\tau} \\ \frac{d(N_{BC\downarrow}(t))}{dt} &= k_{BC0}n_e(t)((\frac{1+DSP}{2}(52.195\%)N_{BC\uparrow} + \frac{1-DSP}{2}(3\%)N_{BC\uparrow}) \\ &-(\frac{1+DSP}{2}(52.195\%)N_{BC\downarrow} + \frac{1+DSP}{2}(3\%)N_{BC\downarrow}))\end{aligned}$$

taking the difference yields

$$\frac{d(dN_{BC0}(t))}{dt} = -k_{BC0}n_e(t)dN_{BC0}(t)((52.195\%)(1+DSP) + (3\%)(1-DSP))$$

The summation of this is

$$\frac{d(sN_{BC}(t))}{dt} = -\frac{sN_{BC}(t)}{\tau}$$

The solution to these are

$$dN_{BC}(t) = dN0_{BC}e^{-\frac{t-tl}{\tau}}(1+(t-tl)\beta n0_h)^{-\frac{k_{BC0}}{\beta}(0.55195+0.49195DSP)}$$
$$sN_{BC}(t) = sN0_{BC}e^{-\frac{t-tl}{\tau}}$$

5.7.3 Diamagnetic Muonium

There is one more species of muonium that needs to be taken into account, the Mu_T^-. This species is considered to be inert since the antimuon spin doesn't change very easily so it won't depolarize over time as it decays. The equations for the Mu_T^- are:

$$\frac{d(dN_{Tm}(t))}{dt} = -\frac{dN_{Tm}}{\tau}$$
$$\frac{d(sN_{Tm}(t))}{dt} = -\frac{sN_{Tm}}{\tau}$$

to which the solutions are

$$dN_{T-}(t) = dN0_{Tm}e^{-\frac{t-tl}{\tau}}$$
$$sN_{T-}(t) = sN0_{Tm}e^{-\frac{t-tl}{\tau}}$$

5.7.4 Laser Off

For the Laser off function, these can be solved by setting $n_e(t) = 0$. The results of these are:

$$dN_{T0}(t) = dN0_{T0}e^{-(t-tl)(\gamma+\frac{1}{\tau})}$$

$$sN_{T0}(t) = sN0_{T0}e^{-\frac{t-tl}{\tau}}$$

$$dN_{BC}(t) = dN0_{BC}e^{-\frac{t-tl}{\tau}}$$

$$sN_{BC}(t) = sN0_{BC}e^{-\frac{t-tl}{\tau}}$$

$$dN_{T-}(t) = dN0_{T-}e^{-\frac{t-tl}{\tau}}$$

$$sN_{T-}(t) = sN0_{T-}e^{-\frac{t-tl}{\tau}}$$

Chapter 6

Analysis and Discussion

The schematic layout for the HiFi spectrometer is shown in Figure 4.2. The antimuon pulse passes the t=0 detector and is implanted into the Si sample about 32ns afterwards. The antimuons are 100% spin polarized in the -z direction, as shown in Figure 4.2. The laser pulse illuminates the sample at a time t_l after the antimuon beam passes the t=0 detector. The time varied for different parts of the experiment, but for most of the experiment it was $t_l = 0.756\mu s$ after the t=0 detector, or $0.720\mu s$ after antimuon implantation. The laser was polarized with either left-handed circularly polarized (LCP) or right-handed circularly polarized (RCP) light. When viewing from the source (the configuration used here), LCP is defined as σ^+helicity while RCP is σ^-. σ^+light has its spin oriented parallel to the direction of propagaion, which is along the -z axis, parallel to the antimuon spin while σ^-light has its spin oriented anti-parallel to its direction of propagation, along the +z axis, anti-parallel to the antimuon spin. The Pockels cell was configured such that when it was turned off, pc off, the light that illuminated the sample was σ^+ and when the Pockels cell was turned on, pc on, the light was σ^-. The DSP that is desired will be found as a difference between σ^- and σ^+ light.

To find where the DSP is the greatest, a wavelength scan of the laser is required. Not only that, but due to the initial polarization of the Mu, as shown in Figures 5.3 and 5.4, a good B-field needs to be chosen as well. If the difference between the electron spin being parallel vs anti-parallel to the antimuon spin is small (red and black curves), the sensitivity of the Mu to the conduction electron spin polarization that has been injected by the laser is low which means only a small portion will be detected. So, the optimal place to search is where or where the average between the two (blue curve) is closest to 50%, At B=0G, the average for Mu^0_T is 50% while the average for Mu^0_{BC} is about 17%. At B=2750G, the average for Mu^0_{BC} is 50% while the average for Mu^0_T is around 95%. This means that the DSP signal should be maximized at a B-field of 0G. However, since the Mu can change sites with the application of the laser, finding out which Mu is responsible for the DSP is much more difficult. It can be seen from Figure 5.4 that at B=2750G and B=-2750G that the polarization of parallel vs anti-parallel are flipped, due to the anisostroy of the Mu^0_{BC} . Therefore, by flipping the B-field direction, the DSP due to the Mu^0_{BC} will also flip sign which means the amount of DSP due to the Mu^0_{BC} can be found. This means that the will also have to be taken at B=2750G and B=-2750G.

6.1 Number of Electron Density in Conduction Band

To calculate the electron density in the conduction band, the first thing is to look at the values of an intrinsic sample. This can be calculated by:

$$n_i = \sqrt{N_c N_v} e^{-\frac{E_g}{2k_B T}}$$

where $N_c = 2.8 * 10^{19}(cm^{-3})$ and $N_v = 1.04 * 10^{19}(cm^{-3})$ at T=300K. In the n-

type sample, the peak photon energy found is 1.176eV (see Section 6.5.2). Assuming that this location is where the T0 phonon turns on, this puts the bandgap at $E_g = 1.176 - 0.019 = 1.156eV$. Plugging this in yields: $n_i = 1.36 * 10^{-126}(cm^{-3})$. It's safe to assume the only conduction band electrons will be from the Phosphorous doping. Next, the number of electrons due to the doping needs to be calculted. To get this, first the total charges available needs to be calculated. The total charges available is N_d=N_d*probability of being occupied + N_c*probability of being occupied (these are the electrons from the impurities that are ionized), where the probability of being occupied is

$$\frac{1}{1 + 0.5e^{\frac{E-E_f}{k_BT}}}$$

Therefore, the total charges available is

$$N_d = \frac{N_d}{1 + 0.5e^{\frac{E_d-E_f}{k_BT}}} + N_C e^{\frac{Ec-Ef}{k_BT}}$$

Solving for this with setting $E_c = 0$ as the reference point:

$$E_f = k_BTLog(\frac{-e^{\frac{E_d}{k_BT}}N_c + e^{\frac{E_d}{2k_BT}}\sqrt{N_c}\sqrt{e^{\frac{E_d}{k_BT}}N_c + 8N_d}}{4N_c})$$

where $N_c = 4.8 * 10^{17}(cm^{-3})$ at T=20K, $N_d = 4.5 * 10^{14}(cm^{-3})$, and $E_d = -0.0445eV$. The solution yields $E_f = -0.0289eV$. Calculating the number of electrons in the conduction band, $n = N_c e^{\frac{E_f}{k_BT}} = 2.59 * 10^{10}(cm^{-3})$. These are excess carriers in the conduction band that can mix with the added carriers by the laser.

6.2 Muonium Hyperfine Frequencies

The Mu hyperfine frequencies in Si have a temperature dependence. The equation that governs the isotropic (Mu_T^0) temperature dependence is [24]:

$$\omega_{T0}(T) = (w_{T0}(0) + \frac{\delta\omega_{T0}}{e^{\Theta'/T}+1}) * (1 - C(\frac{T}{\Theta})^4 \int_0^{\Theta/T} \frac{x^3 dx}{e^x - 1})$$

$$\omega_0(0) = 2006.3MHz$$
$$\delta\omega_{T0} = 31MHz$$
$$\Theta' = 55K$$
$$C = 0.68$$
$$\Theta = 665K$$

Solving for this gives $\omega_{T0} = 2008.2MHz$.

The Mu_{BC}^0 hyperfine frequency can be fit using the equation [37]:

$$A(T) = A(0)(1 - CT^4 \int_0^{\Theta/T} \frac{x^3 dx}{e^x - 1})$$

$$A_\perp(0) = 92.549MHz$$

$$C \perp = 7.136 * 10^{-12}K^{-4}$$

$$A_\parallel(0) = 16.804MHz$$

$$C_\parallel = 3.128 * 10^{-12}K^{-4}$$

$$\Theta = 640K$$

Solving for this yields: $A_\perp = 92.548MHz$ and $A_\parallel = 16.804MHz$.

6.3 α Calculation

The αvalues for each experiment were found by analyzing room temperature (T=298K), TF20, data and are listed in Table 6.1. During the December run, there was a temperature cycle to repair a broken sample thermometer, so $\alpha$was recalculated after this cycle. This value is multiplied to the raw data (the number of positron counts) from the rear detectors before analysis of the data is performed.

Table 6.1: Table of α values

DATE	RUN# (FILENAME)	α
JULY 2015	All	0.962
FEB 2016	All	0.986
DEC 2016	113055-113188	1.055
DEC 2016	113236-113247	1.044
MAY 2017	All	1.055

6.4 Implantation time

The positron decay in the forward and rear detectors are shown in Figures 5.1 and 5.2. Fitting the forward decay to Equation 5.19 with $\tau = 2.197\mu s$, the muon decay time, and $t_p = 0.035\mu s$, half the FWHM of the antimuon pulse. The resulting fit is shown in Figure 6.1.

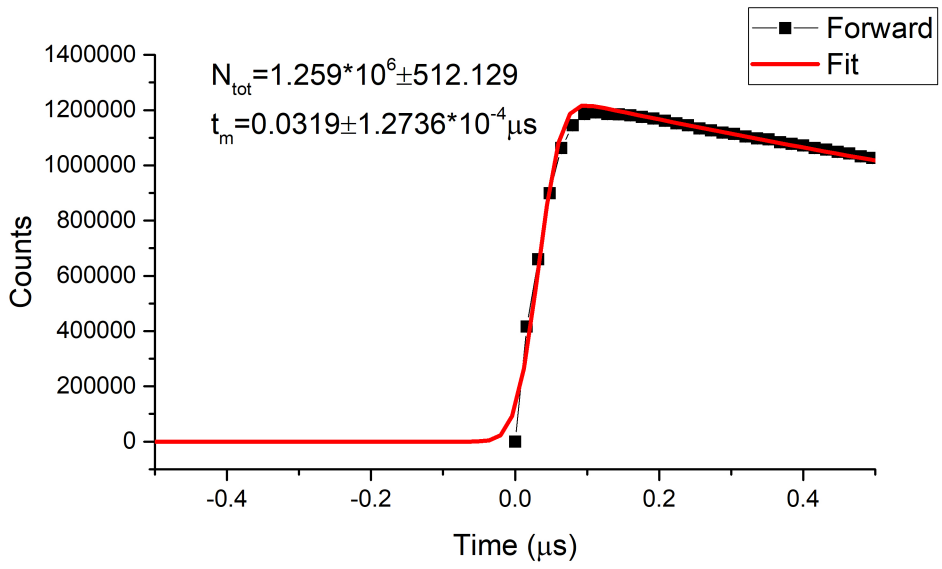

Figure 6.1: Positron decay fit

The value of $t_m$is the implantation time, which can also be found to be the half-way point of the rising edge of the plot. Considering the resolution of the data is 16ns (each bin represents 16ns of time), the closest bin to this is bin 2 at 32ns, which is only 0.032% higher than the fitted results. This implantation time is based off of the ISIS equipment and does not vary throughout the runs.

6.5 N-Type Sample

6.5.1 Asymmetry Data

The asymmetry vs time data, as shown in Equation 5.13, for the wavelength 1054nm from the Feb. 2016 run is plotted in Figure 6.2. The laser on and laser off parts of the graph from t=0 to $t = 0.754\mu s$ are the same since there is no laser present. There is a large drop after the laser hits and it can also be seen that the laser on decay after the laser effect is gone, after $\sim 2.5\mu s$ is slower since the laser off data

starts is closer to the laser on data at $12\mu s$ when compared to $3\mu s$. This represents a slight saturation of the polarization reduction due to the laser.

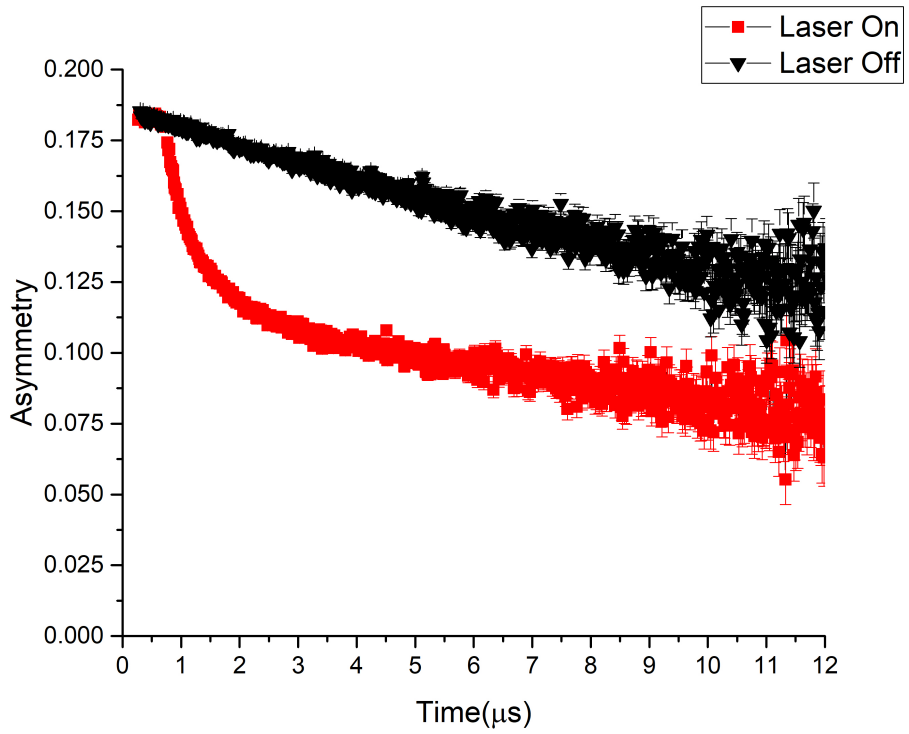

Figure 6.2: Asymmetry vs Time

Figure 6.3 shows the asymmetry vs time plots of σ^- - σ^+ (PC on - PC off respectively). From here, it's impossible to see any difference between the two. This doesn't mean that there isn't a difference, it just means none can be seen at this resolution and a different method must be used.

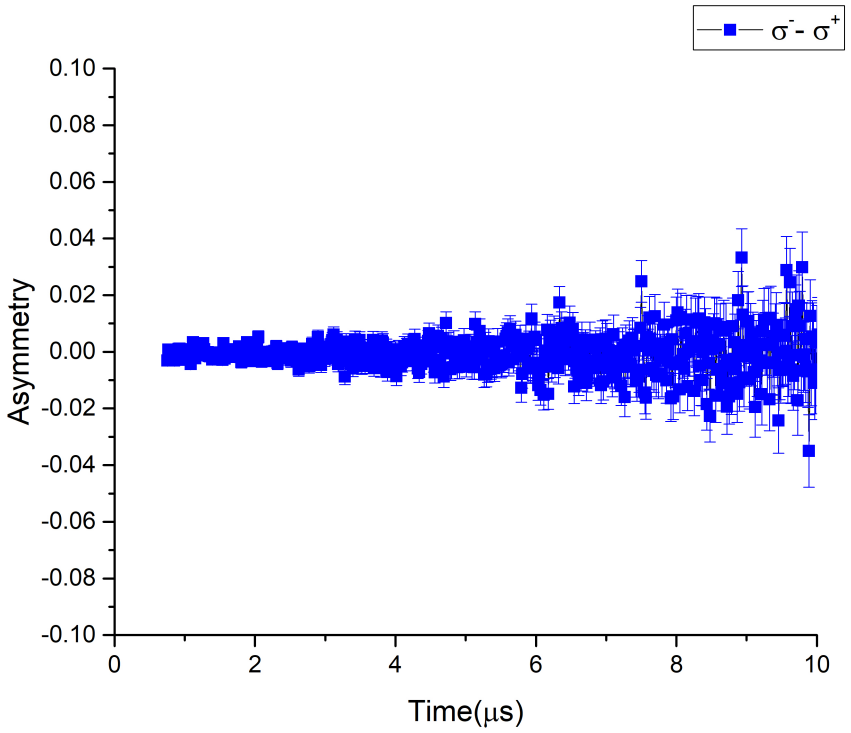

Figure 6.3: Asymmetry v Time of σ^- and σ^+ laser signal

6.5.2 Integration Data

Since the asymmetry vs time data doesn't show any DSP, then another way is to integrate all the σ^- and σ^+raw data, then take the difference. The data is collected in bins, so an a simple summation of the bins is sufficient. The data was taken at B=2750G and repeated with the QWP rotated 90 degrees. The 90 degree rotation flips what channel the σ^+ and σ^- are in. This results in a flip of the sign of the asymmetry value. The integration was performed over the time the laser is present, starting at $t_l = 0.0754\mu s$. The asymmetry is plotted vs the photon energy in Figure 6.4.

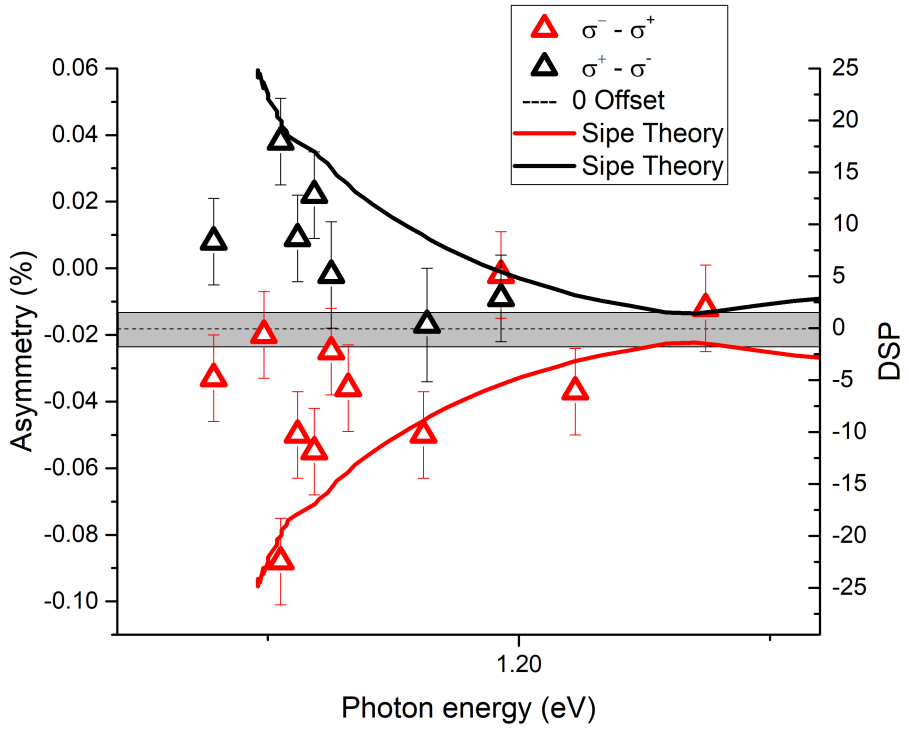

Figure 6.4: DSP vs Photon Energy. There is an offset of $-0.018 \pm 0.0036\%$ with the error indicated by the gray bar.

Takeing the average of the DSP values at each photon energy, then taking the average of these values results in an offset of $-0.018 \pm 0.0036\%$. This offset is expected since the sample has a slight tilt with respect to laser due to the sample mount. The maximum value is -0.088% (-0.070% when taking the offset into account) at the photon energy 1.176eV (1054nm). This data was taken during the Feb 2016 run with the n-type sample. The maximum signal at 1054nm was confirmed with the intrinsic sample during a later run, as shown in Figure 6.15.

6.5.3 Repolarization Curve Fit

In order to find which species of Mu that is sensitive to CESP, the first thing that needs to be found is which species is present and at which amounts. The first experiment done is a B-field scan with no laser present. In the first run at RAL, the B-field was varied throughout the experiment. All the data for laser off is summed up for each B-field since all the parameters for the laser off data were identical, even at different wavelengths. The laser off data is fit to Equation 5.16. The Mu cetners corresponding to the constant A represent centers that are not diffusing within the time frame of the experiment, $32\mu s$ while the centers that correspond to B are diffusing at a rate of α. The most prominent species that are expected in the sample are Mu_T^0 and Mu_{BC}^0. The values of A and B are both plotted with respect to the varying B-field in Figure 6.5. The shapes of these are similar to that of the repolarization curves, with A looking like Figure 5.4 and B looking like 5.3. The sum of these values (A+B) is the initial asymmetry found. This should be equal to the three different species that should be present: Mu_T^0, Mu_{BC}^0, and Mu_T^-. Since $Mu_T^-$is constant at above 10G, the equation for this will be:

$$A_{Tm} + B_{BC}P_{BC}(B) + C_{T0}P_{T0}(BC)$$

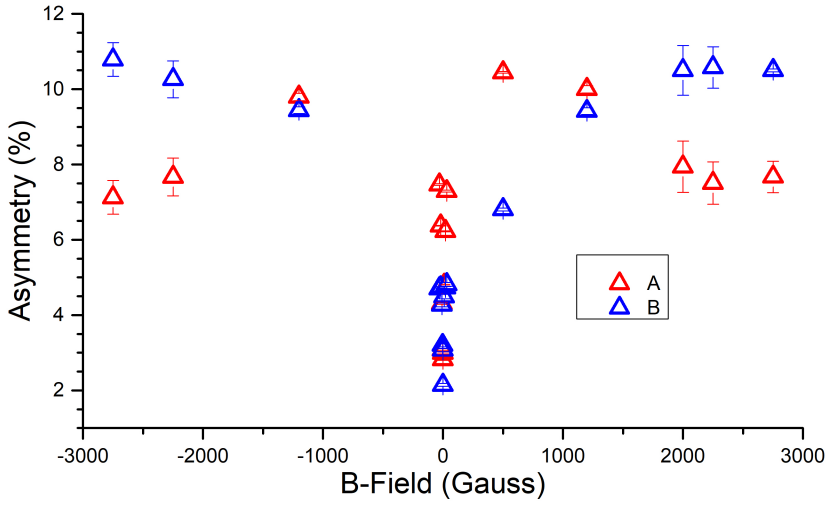

Figure 6.5: Repolarization Curve Fits

This fit will yield the initial amounts of each species. The solution to this fit is in Figure 6.6. The value for A_{Tm} is negative, which is not valid. Breaking up the fit and just fitting the B value to $A' + B'P_{T0}(B)$ yields a fit with the value of A also being negative, as shown in Figure 6.7. There is a portion of B that is constant with the B-field that also decays with γ.

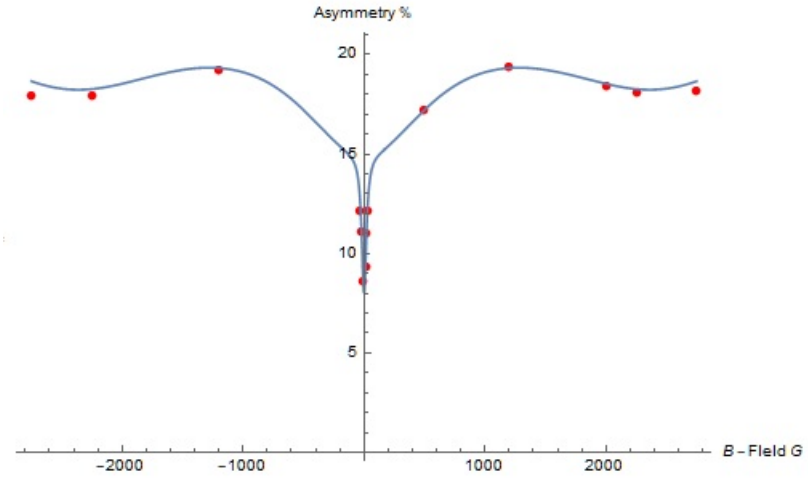

	Estimate	Standard Error	t-Statistic	P-Value
A_{Tm}	−1.28637	0.4243191	−3.031609	0.01141645
B_{BC}	11.57709	0.6191783	18.6975	1.099283×10^{-9}
C_{T0}	14.71506	1.050498	14.00771	2.337271×10^{-8}

Figure 6.6: Fit for sum of Repolarization Curves

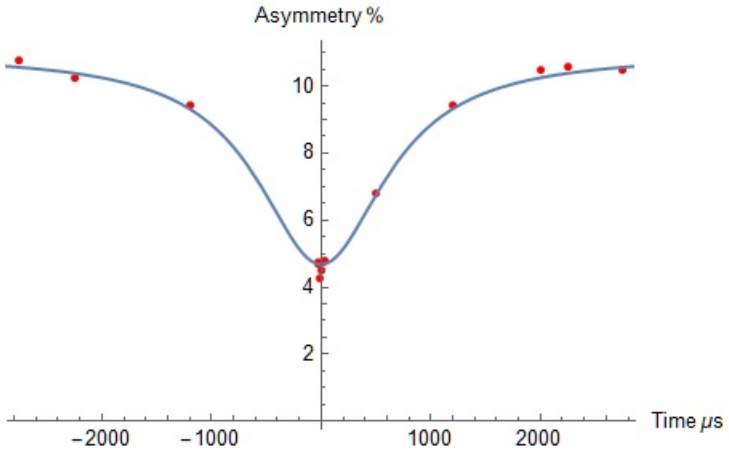

	Estimate	Standard Error	t-Statistic	P-Value
A′	−1.594195	0.1410826	−11.29973	9.422201×10^{-8}
B′	12.55043	0.2385432	52.61284	1.461612×10^{-15}

Figure 6.7: Fit for T-site repolarizaiton curve.

6.5.4 Asymmetry Decay Rate Fit

The constant B in the equation 5.16 matches that of the Mu_T^0 repolarization curve, therefore the decay rate attached to it should also fit with the decay of Mu_T^0 centers. If it doesn't, then it's possible that this decay is a mixture of two or more decay processes that need to be separated out. The data can be fit to Equation 5.8 with constants $\gamma_e = -1.76086 * 10^{11} rad * s^{-1} * T^{-1}$and $\gamma_\mu = 8.51615 * 10^8 rad * s^{-1} * T^{-1}$. The decay rate data is shown in Figure 6.8 along with the fit parameters $v = 1.904 \pm 0.077 (\mu s)^{-1}$ and $\omega = 2\pi * 1908.5 MHz$. This is 5.00% lower than the Mu_T^0 value at 20K of $\omega_{T0} = 2\pi * 2008.1 MHz$. It can be seen from here that the data fits with the decay of Mu_T^0, therefore the constant B can be labeled as Mu_T^0.

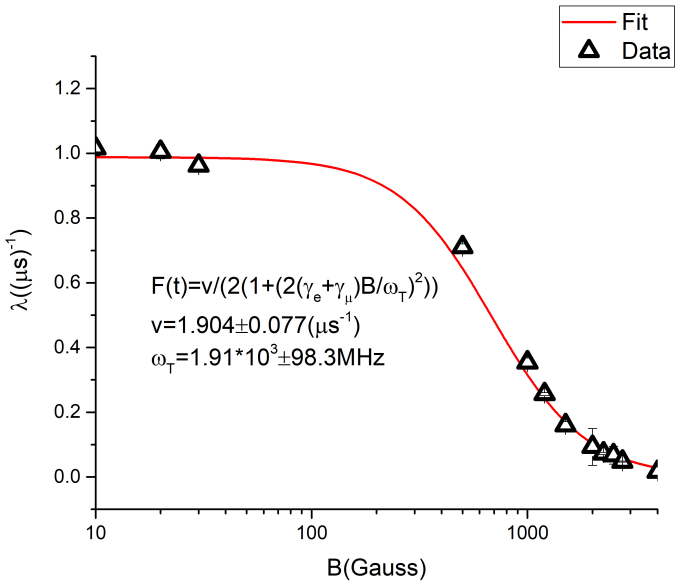

Figure 6.8: Decay Rate of Mu_T^0 centers

There is no decay associated with A. However, that doesn't mean that all of A is a constant that doesn't decay. It's possible that there is a very slow decay that looks like a constant over the time peroid of the experiment. When there is no laser

applied, the amount of excess carriers in the conduction band is $2.59 * 10^{10}(cm^{-3})$, which are due to the Phosphorous dopants. These allow a path for Mu_T^0 to convert to T- via [36]

$$Mu_T^0 + P \rightarrow Mu_T^- + P^+ \tag{6.1}$$

The $Mu_T^0$is mobile, so it can move from site-to-site and collide with the phosphorous dopants, picking up an electron. Therefore, the visible decay in the laser off asymmetry is due to this dopant collision. The Mu_{BC}^0 is not mobile and will therefore merge into the constant A. Eventhough the Mu_{BC}^0spin exchange transition rate, Λ_{BC}^0, is probably high, it still doesn't show up in the asymmetry due to the value of v_{BC}(see equation 5.12) being much lower than the value of v_{PT0} (the spin/charge exchange rate for dopant collision process for Mu_T^0).

6.5.5 Power Dependence

If the laser power is too low, then there will not be enough electrons and holes created by the laser to see the DSP signal within the resolution of the machine. If there's too much laser power, then the sample becomes saturated and all the Mu polarization that's sensitive to photoexcition is stripped away and the asymmetry vs time becomes a flat line, as seen with the 74% laser reduction data in Figure 6.9. There is around a 0.02 asymmetry left over that is not affected by the laser. Since Mu_T^- is considered inert in Si, this leftover is considered to be Mu_T^-.

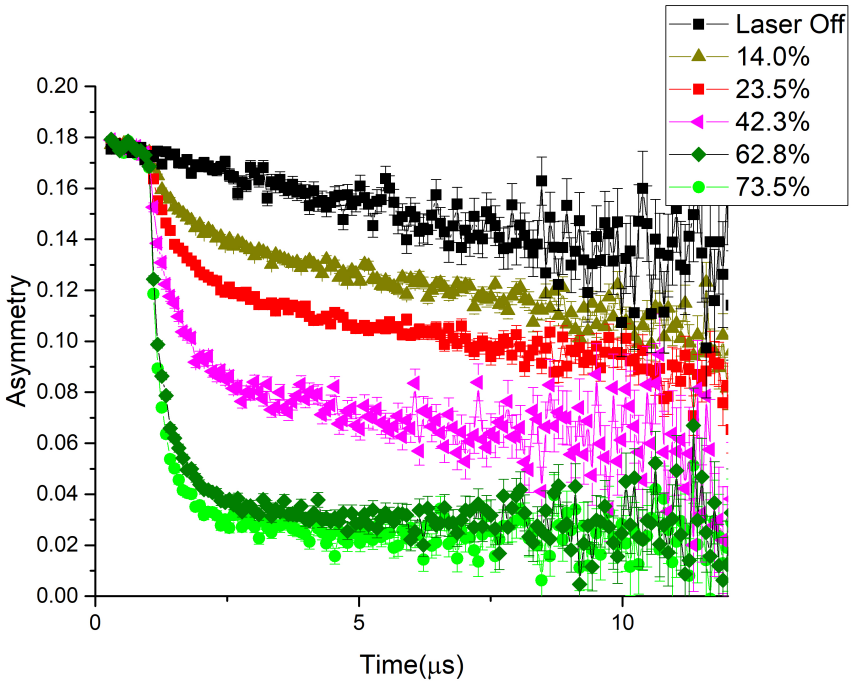

Figure 6.9: Asymmetry vs Time from July 2015 at B=-2750G for various Laser On - Laser Off reductions of $\lambda = 1044nm$ with the N-type sample B=-2750G

The 4 points shown in Figure 6.14 can be used to create a plot of polarization reduction vs laser power on sample, which is shown in Figure 6.10. Unfortunately, there isn't enough data here to do a full analysis of what is happening, but there appears to be a bend in the data that starts at around 30% polarization reduction. Two decays are expected in this data, one from Mu^0_{BC} and another from Mu^0_T. At B=2750G with unpolarized light, the repolarization curve shows that the Mu^0_{BC} is at about 50% polarization while the Mu^0_T is at about 95%. Since the initial Mu^0_T polarization is so much larger than the Mu^0_{BC}, the Mu^0_T will not be as sensitive to the laser as the Mu^0_{BC}. Therefore, the Mu^0_{BC} will depolarize faster than Mu^0_T. The fit function is:

$$F(t) = A(1 - e^{-\alpha t}) + B(1 - e^{\beta t}) \tag{6.2}$$

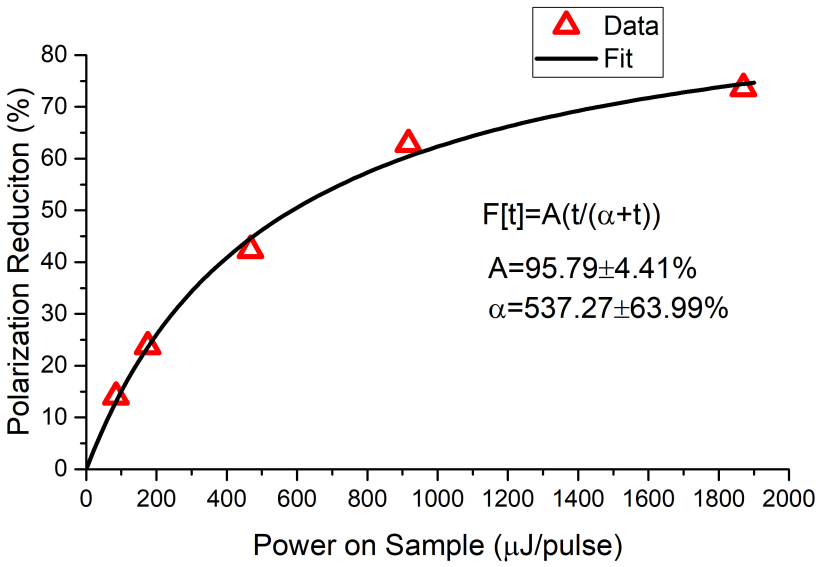

Figure 6.10: Polarization Reduction vs Laser Power for the n-type sample

with the faster decay due to the Mu^0_{BC} and the slower to Mu^0_T. Since there is only 4 data points, this fit can't be done due to it having 4 variables. So, another equation was used to get a clearer image of what is happening (fit function shown in Figure 6.10). This bend shows that there is a saturation point where the Mu starts to become less and less sensitive to the laser. The optimal location for the experiment will be right at the start of this bend, at the end of the linear regime, at the 30% polarization reduction. This is where the wavelength dependent scan took place.

6.5.6 Model Fit

Since the asymmetry equations looks like Equation 5.13, the asymmetry equation for laser on can be created with the model created in Section 5.7 as:

$$A(t) = a(P(t))$$

$$P(t) = \frac{\frac{dN_{T0}(t)+dN_{BC}(t)+dN_{Tm}(t)}{sN_{T0}(t)+sN_{BC}(t)+sN_{Tm}(t)}}{\frac{dN_{T0}(tl)+dN_{BC}(tl)+dN_{Tm}(tl)}{sN_{T0}(tl)+sN_{BC}(tl)+sN_{Tm}(tl)}}$$

where P(t) is normalized to 1 when the laser is applied. A plot of this along with a plot of the model for laser off is shown in Figure The polarization functions for each species can be written as:

$$P_{T0}(t) = \frac{dN_{T0}(t)}{sN_{T0}(t)}$$
$$P_{BC}(t) = \frac{dN_{BC}(t)}{sN_{BC}(t)}$$
$$P_{T0}(t) = \frac{dN_{Tm}(t)}{sN_{Tm}(t)}$$

A plot of these polarizations is shown in Figure 6.11.

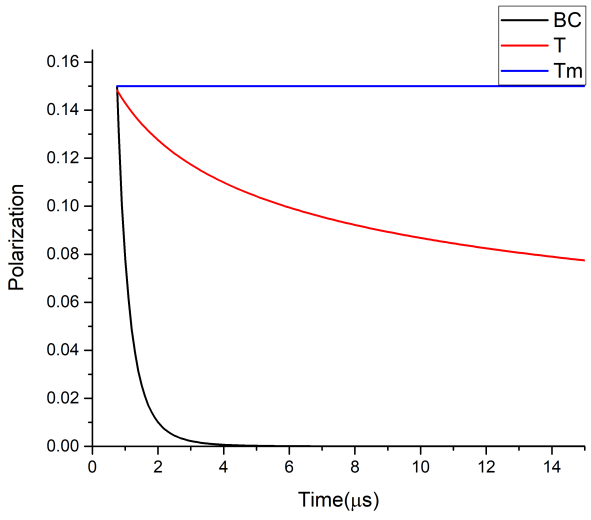

Figure 6.11: Polarization plot of Mu^0_{BC}, Mu^0_T, and Mu^-_T.

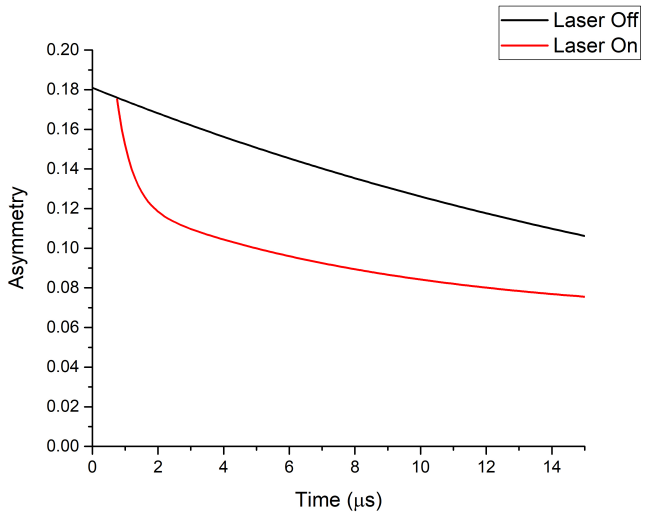

Figure 6.12: Plot of the laser on and laser off models.

There are a total of 7 variables to fit. However, since In order to reduce the amount of variables, some reductions can be made. First, since we are assuming no site or charge cycles, the asymmetry equation can be broken up into a summation of the Mu_T^0, Mu_{BC}^0, and Mu_T^- polarization functions. The summation $A + B$, which is the total amount of initial asymmetry, can be written as:

$$nBC * P_{BC}(0) + nT * P_T(0) + (1 - nBC - nT) \tag{6.3}$$

where $nBC * P_{BC}(0) + (1 - nBC - nT)$ is equal to A (with $(1 - nBC - nT)$ equal to the amount of Mu_T^-) and $nT * P_T(0)$ is equal to B. The laser on asymmetry can be written as:

$$(A + B) * (nBC * P_{BC}(t) + nT * P_T(t) + (1 - nBC - nT))/ \tag{6.4}$$
$$(nBC * P_{BC}(tl) + nT * P_T(tl) + (1 - nBC - nT))$$

Equation 6.3 can be set equal to $B/(A+B)$ and solved for nT. Plugging this into Equation 6.4:

$$(-B*nBC*P_{BC}(tl)+B*nBC*P_{BC}(t)+A*P_T(t)+$$
$$A*nBC(-1+P_{BC}(t))*P_T(tl)+B(1+nBC(-1+$$
$$P_{BC}(tl)))P_T(t))/(1+nBC(-1+P_{BC}(0))P_T(0)))$$

A and B are taken from the laser off fits and nBC is a fit variable. The polarization functions for Mu_T^0, Mu_{BC}^0, and Mu_T^- can be simplified to be:

$$P_T(t) = 0.969e^{-\gamma t}(1+\beta n0_e(t-tl))^{-0.031\beta k_T}$$
$$P_{BC}(t) = 0.496(1+(t-tl)\beta n0_e)^{(-0.5-0.5DSP)\beta k_{BC}}$$
$$P_{Tm}(t) = 1$$

whereβ is absorbed into $n0_e$,k_T, and k_{BC}. This reduces the amount of variables down to 4; $n0_e$,k_T,nBC, and k_{BC} However, since there is an issue with the fits of the repolarization curves (see Section 6.5.3), the amounts of Mu_T^0, Mu_{BC}^0, and Mu_T^- haven't been found confidently, so they must now be free variables. This brings the amount of variables up to 6. Since this is the same amount of to the peak signal from Figure 6.4 yields:

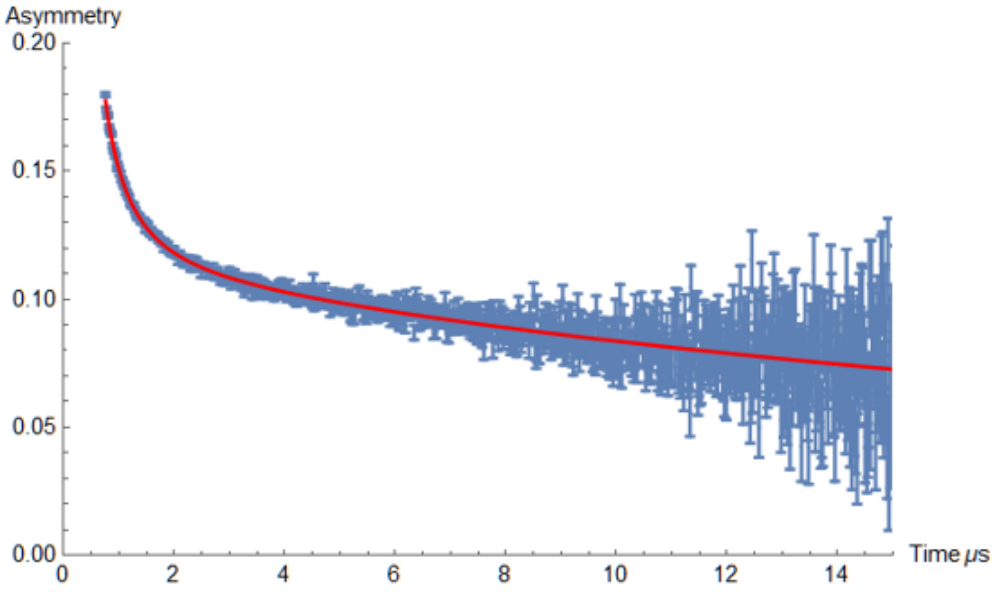

	Estimate	Standard Error
$a\beta n0_e$	0.0003391719	0.04701549
nBC	0.4602724	0.00366717
βk_T	7236.768	1.004397×10^6
βk_{BC}	12920.21	1.790792×10^6
B	0.05854257	0.008068094
A	0.1167722	0.007927583

Figure 6.13: Model fitting to laser on at $\lambda = 1054nm$.

The errors are large, so no information about where the DSP will come from can be extracted, but the function does fit well to the data so these values can be used to get an extracted DSP.

6.5.7 Integral Fit

The integral analysis is an integration of the detector counts, then the asymmetry is taken. So, this has to be re-created using the model in order to extract the DSP. The integration of the laser on data can be completed using

$$IA = aIP = \frac{\frac{\int_{0.752}^{20.272}(dN_{T0}(t)+dN_{BC}(t)+dN_{Tm}(t))dt}{\int_{0.752}^{20.272}(sN_{T0}(t)+sN_{BC}(t)+sN_{Tm}(t))dt}}{\frac{\int_{0.752}^{20.272}(dN_{T0}(tl)+dN_{BC}(tl)+dN_{Tm}(tl))dt}{\int_{0.752}^{20.272}(sN_{T0}(tl)+sN_{BC}(tl)+sN_{Tm}(tl))dt}} \tag{6.5}$$

where each term can be integrated separately due to the additive property of integrals. Then, to re-create the asymmetry difference shown for the peak wavelength 1054 in Figure 6.4 (-0.0709%), $\sigma^- - \sigma^+$, Equation 6.5 will be used for each σ^- and σ^+ with the DSP in σ^+ set to +DSP and σ^- is set to -DSP and the values for the coefficients found in Section 6.5.6 plugged in. With a DSP of 1.59%, the value of $\sigma^- - \sigma^+$ from the model is -0.0708%. Therefore, the extracted DSP is 1.59%.

6.6 Intrinsic Sample

6.6.1 Power Dependence

Figure 6.14 shows the polarization reduction due to the laser vs laser power. This data was taken with the intrinsic sample. There plot is linear between 0-15% reduction. After this, a saturation occurs due to a reduction of certain species of Mu no longer being sensitive to the laser. Therefore, the optimal place to scan is just before the "knee" of the graph at about 17.5% reduction. This value is less than in the n-type sample. Also, the full saturation point is significantly less than in the n-type sample as well with saturation peaking at about 35% polarization reduction while in the n-type full saturation occurs at around 75%.

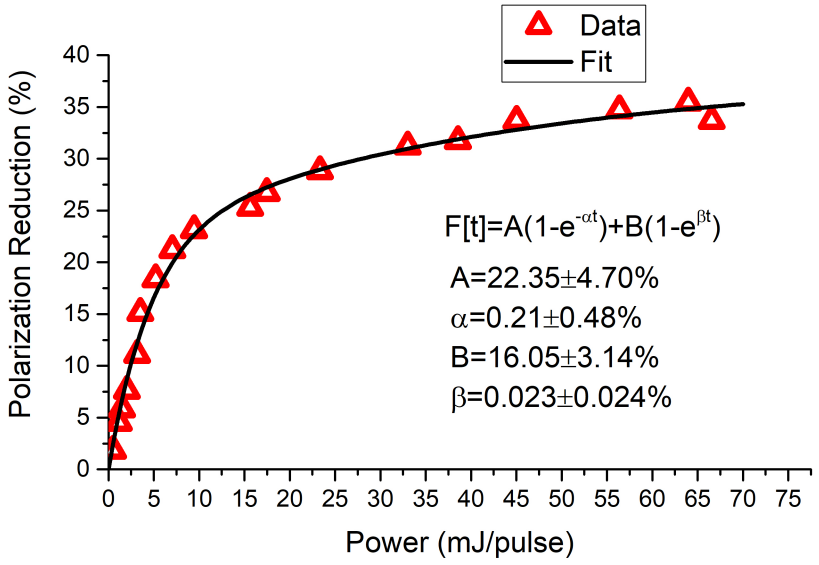

Figure 6.14: Polarization Reduction vs Laser Power for the intrinsic sample

Figure 6.15 shows the spin-dependent asymmetry vs polarization reduction at the peak wavelength, 1054nm for the intrinsic sample. The B-field was also flipped between +2750G and -2750G. The data from the n-type sample with the same settings is also in the graph. If any of the spin polarization signal is derived from the Mu^0_{BC} , then one direction of the B-field will cause an addition to the spin-depent asymmetry while the other direction will cause a subtraction. If a difference was to be seen, then this could be used to retrieve the amount of spin-dependent asymmetry that was contributed by the Mu^0_{BC} . There appears to be a difference in the data at 22% polarization reduction that is mirrored with the B-field flip. It's possible that this is an actual change due to the Mu^0_{BC} , however the error bars are large enough that it's not conclusive. Looking at Figure 6.14, the start of the saturation begins at around 17.5% polarization redcution. There is only one data point in Figure 6.15 that is in this linear regime. The rest of the points lie either within the bend or on the other side. With the Mu^0_{BC} being almost or completely destroyed by the laser, and the

Mu^0_{BC} population being about half the size as the Mu^0_T population, it's not expected to see the flipping of the Mu^0_{BC} due to the magnetic field, especially considering the error bars. Since we are in this regime, it can be noted that the spin dependence will come from Mu^0_T.

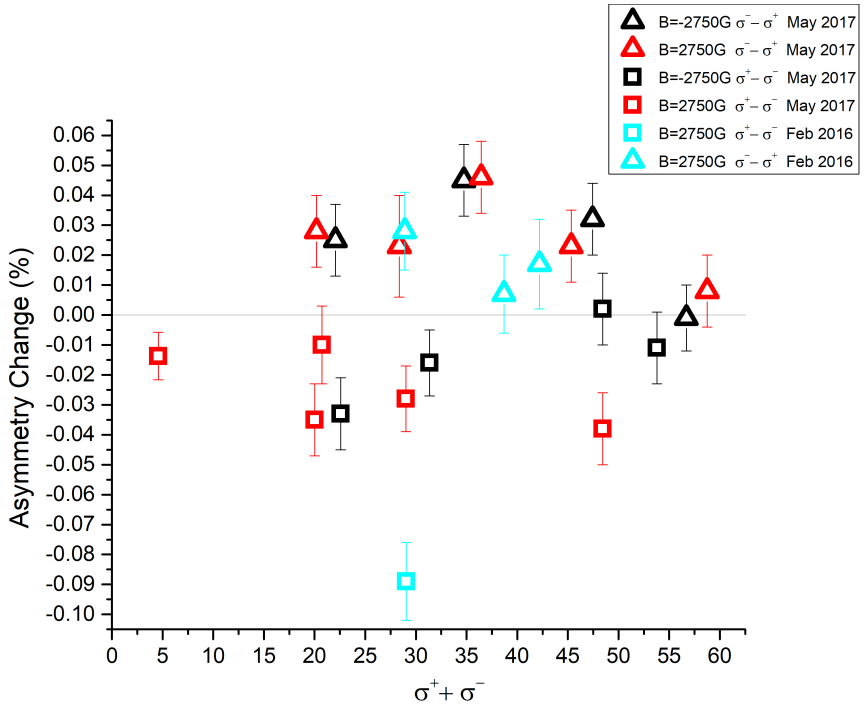

Figure 6.15: DSP vs Polarization Reduciton.

Chapter 7

Conclusion

The optical injection of spin polarization into n-type and intrinsic Si have been studied using a muon spin relaxation technique [9]. The results have shown that the irradiation due to the laser has caused not only a unpolarized laser effect, but also a smaller polarized laser effect. The unpolarized laser effect is due to the different processes that occur when the muons are subjected to a large amount of excess electron and hole carriers which can occur regaurdless of whether or not there is any polarization of the excess carriers that are created. Some of these processes can also be altered with the polarization of the excess carriers due to the hyperfine coupling of the Mu. The laser power, amount of excess carriers created, has also been shown to alter not only the unpolarized laser offect but the polarized laser effect as well. Too much laser power will saturate and dispose of any polarization that is sensitive to the laser sample while too little laser power will yield a result that is too small to see within the error bars.

The amount of asymmetry from the experiment is significantly smaller, -0.06%, than the theoretical predictions of DSP, -25%. This discrepincy has to do, in part, with the Mu processes that occur in Si. First, we have shown that not all the Mu

polarization is sensitive to the laser. Secondly, at the B-fields that were ran, not all the Mu is sensitive to the hyperfine coupling. Taking these into account, a model that considers the most significant of the processes was created to extract the DSP from the asymmetry which are the spin exchanges with the Mu^0_{BC} and Mu^0_T species as well as the conversion of Mu^0_T to Mu^-_T due to collisions with the Phosphorous dopants. Using the model, the extracted DSP is 1.59% with the majority of the DSP coming from the Mu^0_T species, which is also smaller than the theoretical predictions and also the opposite sign.

Bibliography

[1] Georges Lampel. Nuclear Dynamic Polarization By Optical Electronic Saturation And Optical Pumping In Semiconductors. *Physical Review Letters*, 20(10), March 1968.

[2] Ian Appelbaum, Biqin Huang, and Douwe J. Monsma. Electronic Measurement And Control Of Spin Transport In Silicon. *Nature*, 447:295–298, 2007.

[3] B. T. Jonker, Y. D. Park, B. R. Bennett, et al. Robust Electrical Spin Injection Into A Semiconductor Heterostructure. *Physical Review B*, 2000.

[4] R. Fiederling, P. Grabs, W. Ossau, G. Schmidt, and L. W. Molenkamp. Detection Of Electrical Spin Injection By Light-emitting Diodes In Top- And Side-emission Configurations. *Applied Physics Letters*, 2003.

[5] H. J. Zhu, M. Ramsteiner, H. Kostial, et al. Room-temperature Spin Injection From Fe Into GaAs. *Physical Review Letters*, 2001.

[6] B.T. Jonker, George Kioseoglou, Aubrey T. Hanbicki, Connie H. Li, and Phillip E. Thompson. Electrical spin-injection into silicon from a ferromagnetic metal/tunnel barrier contact. *Nature Physics*, 3:542–546, 2007.

[7] J. L. Cheng, M. W. Wu, and J. Fabian. Theory of Spin Relaxation of Conduction Electrons in Silicon. *Physical Review Letters*, 104, January 2010.

[8] B. I. Zakharchenya, V. G. Fleisher, R. I. Dzhioev, Yu. P. Veshchunov, and I. B. Rusanov. Effect Of Optical Orientation Of Electron Spins In A GaAs Crystal. *JETP Letters*, 1971.

[9] Koji Yokoyama. *Muon Probes Of Spin-polarized Electrons In GaAs*. PhD thesis, University of Riverside, California, 2009.

[10] M. Inglot, V.K. Dugaev, E. Ya Sherman, and J. Barnas. Optical spin injection in graphene with Rashba spin-orbit interaction. *Physical Review B*, 2014.

[11] E. Torikai, Y. Ikedo, K. Shimomura, et al. Interaction of Mu With Spin Current in GaAs/GaAsP/Si. *Physica B: Condensed Matter*, 289:558–562, August 2000.

[12] Biqin Huang, Douwe J. Monsma, and Ian Applebaum. Coheren Spin Transport Through A 350 Micron Thick Silicon Wafer. *Physical Review Letters*, 99, 2007.

[13] Wikipedia. Bangdap. https://en.wikipedia.org/wiki/Band_gap.

[14] Wikipedia. Brillouin Zone. https://en.wikipedia.org/wiki/Brillouin_zone.

[15] Conduction Band Valleys. http://www.iue.tuwien.ac.at/phd/dhar/node18.html.

[16] R. J. Elliott. Theory of the Effect of Spin-Orbit Coupling on Magnetic Resonance in Some Semiconductors. *Physical Review*, 96(2), 1954.

[17] Y. Yafet. *Solid State Physics*. Academic, New York, 1963.

[18] D. J. Lepine. Spin Resonance of Localized and Delocalized Electrons in Phosphorus-Doped Silicon between 20 and 30 Â°K. *Physical Review B*, 1970.

[19] G Lancaster, J.A. Van Wyk, and E.E. Schneider. Spin-lattice Relaxation of Conduction Electrons in Silicon. *Proc Phys Soc*, 1964.

[20] J. H. Pifer. Microwave Conductivity And Conduction-electron Spin-resonance Linewidth Of Heavily Doped Si:p And Si:As. *Physical Review B*, 12(10), November 1975.

[21] Toshio Suzuki, Tomoyuki Sasaki, Tohru Oikawa, et al. Room-temperature Electron Spin Transport In A Highly Doped Si Channel. *Applied Physics Express*, 4(2), February 2011.

[22] Ron Jansen. Silicon Spintronics. *Nature Materials*, 11:400–408, April 2012.

[23] J. L. Cheng, J. Rioux, J. Fabian, and J. E. Sipe. Theory Of Optical Spin Orientation In Silicon. *Physical Review B*, 83, April 2011.

[24] Eugen Holzschuh. Direct measurement of muonium hyperfine frequencies in Si and Ge. *Physical Review B*, 1983.

[25] Bruce D. Patterson. Muonium States In Semiconductors. *Reviews of Modern Physics*, 60(69), 1988.

[26] R.F. Kiefl, M Ceilo, T.L. Estle, et al. Si Hyperfine Structure of Anomalous Muonium in Silicon: Proof of the Bond-Centered Model. *Physical Review Letters*, 1988.

[27] S. R. Kreitzman, B. Hitti, R. L. Lichti, T. L. Estele, and K. H. Choe. Muon-spin-resonance Study Of Muonium Dynamics In Si And Its Relevance To Hydrogen. *Physical Review B*, 51(19):117–137, January 1995.

[28] K Yokoyama, J.S. Lord, J. Miao, P. Murahari, and A.J. Drew. Photoexcited Muon Spin Spectroscopy: A New Method for Measuring Excess Carrier Lifetime in Bulk Silicon. *Physical Review Letters*, 119(226601), 2017.

[29] I Fan, K.H. Chow, B. Hitti, et al. Optically Induced Dynamics of Muonium Centers in Si Studied Via Their Precession Signatures. *Physical Review B*, 77, 2008.

[30] I. Fan, K. H. Chow, M. Egilmez, et al. Muonium Dynamics in Doped Si Probed by Photoexcited TF-muSR Measurements. *Physica B: Condensed Matter*, 404:852–855, 2009.

[31] Alain Yaouanc and Pierre Dalamas de Reotier. *Muon Spin Rotation, Relaxation, and Resonance*. Oxford University Press, 2011.

[32] J. S. Lord. Computer Simulation Of Muon Spin Evolution. *Physica B: Condensed Matter*, 2006.

[33] O. Arnold, J.C. Bilheux, J.M. Borreguero, et al. Mantid - Data Analysis and Visualization Package for Neutron Scattering and muSR Experiments. *Phys. Res.*, 2014.

[34] K. Yokoyama, J. S. Lord, P. Murahari, et al. The New High Field Photoexcitation Muon Spectrometer At The Isis Pulsed Neutron And Muon Source. *Review of Scientific Instruments*, 87(12), 2017.

[35] F.L. Pratt. WIMDA: a muon data analysis program for the Windows PC. *Physica B: Condensed Matter*, 2000.

[36] R. Kanado, R. M. Macrae, and K. Nagamine. Charge Dynamics Of Muonium Centers In Si Revelaed By Photoinduced Muon Spin Relaxation. *Physical Review B*, 68, 2003.

[37] K.W. Blazey, J.A. Brown, D.W. Cooke, et al. Temperature Dependence of the

Anomalous Muonium Hyperfine Interaction and Depolarization Rate in Silicon. *Physical Review B*, 1981.